1   **Quantitative investigation of gas flow, powder-gas interaction, and powder behavior under**

2   **different ambient pressure levels in laser powder bed fusion**

3

4   **Abstract**

5   The powder motion in laser powder bed fusion (LPBF) processes cause defect and variability

6   issues in the built products. It has been reported that the ambient pressure has a significant

7   influence on the powder motion, but the physical effects of the ambient pressure on the gas flow,

8   powder-gas interaction, and powder behavior are not quantitatively understood. In this work, we

9   have developed the first three-dimensional multiphysics model for LPBF to simulate the molten

10   pool dynamics, depression zone evolution, gas flow structure, and powder motion in a fully

11   coupled manner. The model enables the first quantitative investigation of the gas flow, powder-

12   gas interaction, and powder behavior in LPBF with different ambient pressure levels, all of which

13   are difficult to measure by experiments. The simulation results show a consistent gas flow structure

14   for all different pressure levels, but the gas flow parameters (temperature, velocity, Reynolds

15   number, and Knudsen number) vary significantly with the ambient pressure. Four powder-gas

16   interaction modes are defined by the gas flow around the particle and the gas-induced forces on

17   the particle, and the interaction modes, individually or collectively, control the motion of each

18   particle. With the changes in the ambient pressure and the gas flow parameters, the significance of

19   the four modes to the powder motion varies, and the powder behavior (temperature, force, velocity,

20   and ejection angle) becomes different. A new strategy is proposed to mitigate the powder motion

21   based on the modeling results.

22

23 **Keywords**

24 Laser powder bed fusion; Gas flow; Powder motion; Multiphysics modeling; High-speed X-ray

25 imaging.

26

27 <mark>Nomenclature</mark>

ρ: Density

$\vec{V}$: Velocity

t: Time

p: Pressure

τ: Viscous stress

μ: Viscosity

$\vec{g}$: Gravity

$\vec{S}_D$: Darcy's term

e: Total energy

k: Thermal conductivity

T: Temperature

Y: Mass fraction of metal vapor

D: Diffusivity of metal vapor

K_D: Resistance function in Darcy's term

ϕ: Levelset function

λ: Mean free path

R_s: Specific gas constant

V_{ct}: Tangential velocity in the condensed phase

V_{gt}: Tangential velocity in the gaseous phase

σ_v: Tangential momentum accommodation coefficient

m_p: Particle mass

$\vec{V}_{pc}$: Velocity at particle center

$\vec{F}_f$: Fluid-induced force on particle

$\vec{F}_{col}$: Collision force on particle

I_p: Moment of inertia of particle

$\vec{\omega}_p$: Angular velocity of particle

α_k: Spring coefficient for particle collision

α_d: Damping coefficient for particle collision

E: Young's modulus

ν: Poisson ratio

ζ: Damping coefficient

28

1. Introduction

30   Laser powder bed fusion (LPBF) is a mainstream additive manufacturing technology in which

31   a laser selectively fuses metal powder particles layer-by-layer to print three-dimensional builds.

32   Although LPBF has shown promising capabilities of achieving complex and flexible geometries

33   to a designer's needs, there are defects and variability issues that inhibit further adaptation of this

34   emerging manufacturing method. One major cause of the defects and print variability is the gas-

35   flow-induced powder motion in LPBF. It has been reported in the literature that laser heating

36   triggers strong evaporation on the metal surface. The vapor flux forms a vapor jet and entrains the

37   surrounding gas, creating a complex gas flow, and eventually, the powder-gas interaction drives

38   the powder motion [1]. It is observed that the powder particles have a tendency of being entrained

39   towards and then ejected from the laser-illuminated zone (LIZ) [2, 3]. The entrainment dislocates

40   the powder particles originally deposited around the LIZ [4]. The uniformity of the powder

41   distribution is disrupted, which leads to the variability of builds from print to print. More

42   importantly, the powder ejection gives rise to airborne spatters in solid or liquid form [5]. The

43   spattering leads to a series of deleterious effects, including degraded surface roughness [6], lack-

44   of-fusion [7], increased oxidation [8], and inhomogeneity of the feedstock [9], all of which

45   contribute to poor mechanical properties in the final build [10].

46   Research efforts have been motivated to study the effects of process conditions on the powder

47   motion in LPBF, in the hope that the powder motion can be mitigated, if not fully controlled. The

48   investigated process conditions include varying the laser power and scanning speed [2, 11], the

49   ambient gas pressure [12-14] and composition [15, 16], as well as applying a cross-flow in the

50   build chamber [17]. Among these conditions, varying the ambient gas pressure is found to

51   influence the powder motion dramatically. It is reported in [13] that the numbers of the entrained

52   and ejected powder particles increase as the ambient pressure is decreased below the atmospheric

53   pressure (1 bar). Under extremely low ambient pressure (smaller than 1 mbar), few particles can

54   be entrained near the LIZ, and the particles surrounding the LIZ are mostly ejected. Similar

55   observations are reported in [12] where the authors correlate the ambient pressure with the vapor

56   jet divergent angle and the powder motion. Apparently, extremely low ambient pressure leads to

57   a large amount of ejected powder particles and therefore should be avoided. The authors in [18]

58   explored the window of ambient pressure between 10 mbar to 1 bar and found that 200 mbar

59   achieves a similar amount but less variability of spattered particles. For the ambient pressure higher

60   than the atmospheric pressure, the only study found in the literature is [14]. This rareness might

61   be explained by the difficulty of building a high-pressure chamber. According to [14], the number

62   of entrained particles is decreased as the ambient pressure is increased above 1 bar, but the number

63   of ejected particles is increased. The authors suggested that high ambient pressure does not have

64   an advantage in reducing the powder motion.

65   There is a large parameter window (laser power, scanning speed, ambient pressure, etc.) from

66   which one can identify the optimal parameter combinations to mitigate the powder motion. In that

67   regard, the underlying physics of the powder-gas interaction needs to be fully understood to

68   minimize the costly trial-and-error tests to identify the optimal conditions. The high-speed X-ray

69 and optical imaging are capable of visualizing and tracking the powder motion with high spatial

70 (up to 1 μm) and temporal resolution (up to 1 μs). However, quantitative information regarding

71 the powder-gas interaction, i.e., the gas flow surrounding the powder particles and the forces

72 exerted on the particle surfaces, is difficult to measure experimentally. In this regard, multiphysics

73 simulations can be a complement to the imaging techniques to determine these quantities.

74 Multiphysics simulations have been extensively utilized to study the molten pool behavior in

75 LPBF. The simulated phenomena include the laser-metal interaction [7], molten pool flow [19],

76 pore formation [20], keyhole instability [21], and lack-of-fusion development [22, 23]. There are

77 relatively fewer efforts for gas flow simulations in LPBF. The vapor jet expansion and the

78 entrainment flow were simulated in [2] but the thermal-fluid coupling between the gas and the

79 molten pool was ignored. This coupling was added in a later study [24], but the simulation did not

80 track the powder motion. Powder particles are typically either ignored or assumed to be sintered

81 to the substrate. In a recent publication [25], the gas flow and powder motion were simulated, but

82 the gas flow was decoupled with the molten pool dynamics. The vapor jet was artificially defined,

83 and the effects of the jetting angle on the powder motion were investigated. In a previous

84 publication [26], we developed a two-dimensional (2D) model that fully coupled the molten pool

85 dynamics, gas flow, and powder motion. However, the phenomena in the third dimension were

86 ignored, which can compromise the fidelity of the simulation results.

87 In an attempt to further improve the fidelity of multiphysics simulations, we extend our

88 previous 2D model to a three-dimensional (3D) model in this work. Particularly, the 3D model is

89 used to investigate the effects of the ambient pressure on the gas flow, powder-gas interaction, and

90 powder behavior. The simulation results are validated against high-speed X-ray imaging

91 experiments. The model predictions of gas pressure, velocity, and temperature, as well as the

92   powder quantities such as force, velocity, and temperature, are identified as functions of the

93   ambient pressure, which are used to quantitatively understand the underlying physics under

94   different ambient pressure levels.

95   **2. Methods**

96   *2.1 Multiphysics simulation*

97   The calculation domain for the multiphysics simulation consists of the condensed phase region

98   and the gaseous phase region. The condensed region includes the substrate, molten pool, and the

99   individual powder particles. The gaseous region includes the metal vapor due to evaporation and

100   the ambient protection gas (typically argon). The interface between the condensed and gaseous

101   region is referred to as the C-G interface. The calculation domain is discretized into a Cartesian

102   mesh, and variables are computed at each cell of the mesh using computational fluid dynamics

103   (CFD) methods. Both the condensed and gaseous regions are subject to CFD computation. The C-

104   G interface is captured by the level-set method. The individual particles are tracked by the discrete

105   element method (DEM). The CFD and DEM computations are fully-coupled and carefully

106   coordinated to model the powder-gas interaction. The modeling methodology of the current model

107   is consistent with our previous model, with the dimension extended from 2D to 3D. The methods

108   are briefly described here, and more details can be referred to [26-29].

109   The governing equations for the CFD computation are the conservation equations of mass,

110   momentum, energy, and the vapor species:

$$\frac{\partial \rho}{\partial t} + \nabla \cdot \left(\rho \vec{V} \right) = 0 \tag{1}$$

$$\frac{\partial (\rho V)}{\partial t} + \nabla \cdot \left(\rho \vec{V} \vec{V} \right) = -\nabla p + \nabla \cdot \tau + \rho \vec{g} + \vec{S}_D \tag{2}$$

$$\frac{\partial (\rho e)}{\partial t} + \nabla \cdot \left(\rho e \vec{V} \right) = -\nabla \cdot \left(p \vec{V} \right) + \nabla \cdot \left(\tau \cdot \vec{V} \right) + \rho \vec{g} \cdot \vec{V} + \nabla \cdot (k \nabla T) \tag{3}$$

$$\frac{\partial(\rho Y)}{\partial t} + \nabla \cdot \left(\rho Y \vec{V}\right) = \nabla \cdot (\rho D \nabla Y) \tag{4}$$

111   Here, Eq. (1) is the mass conservation equation where ρ is the density, $\vec{V}$ is the velocity, and t is

112   the time. Eq. (2) is the momentum conservation equation where p is the pressure, τ is the viscous

113   stress tensor, $\vec{g}$ is the gradational vector, and $\vec{S}_D$ is the Darcy's term. Eq. (3) is the energy

114   conservation equation where e is the total energy (internal and kinetic energy), and k is the thermal

115   conductivity. Eq. (4) is the vapor species conservation equation where Y is the mass fraction of the

116   metal vapor in the gaseous region, and D is the diffusion coefficient of the vapor. It is assumed

117   that the condensed region is a continuum with only one species (metal), and the gaseous region

118   has two species, metal vapor and argon gas. Eq. (4) is only solved in the gaseous region. The

119   Darcy's term is written as:

$$S_D = -K_D(T)\left(\vec{V} - \vec{V}_s\right) \tag{5}$$

120   In Eq. (5), $\vec{V}_s$ is a solid velocity. It is assigned to be the particle velocity if the cell is inside a powder

121   particle, and is assigned to be zero otherwise. K_D is a function of temperature T. It is a large

122   number if T is below the solidus temperature, is equal to zero if T is above the liquidus temperature,

123   and is smoothed connected if T is in between. With Eqs. (1)-(4), the pressure, velocity, temperature,

124   and vapor mass fraction can be obtained at each cell center by the CFD computation.

125   The evolution of the C-G interface is governed by the level-set advection equation:

$$\frac{\partial \phi}{\partial t} + \vec{V} \cdot \nabla \phi = 0 \tag{6}$$

126   In Eq. (6), ϕ is the level-set function. ϕ is defined to be the signed distance to the interface, and

127   the zero-level-set isosurface represents the C-G interface. Once the C-G interface is identified, the

128   ghost fluid method is applied to separate the calculation domain into the condensed and gaseous

129 region. The boundary conditions are carefully defined at the C-G interface to capture the interface

130 phenomena, including the surface tension, thermal-capillary (Marangoni) effect, recoil pressure,

131 and evaporation vapor flux.

132 Different from our previous model, a slip boundary condition is implemented in the current

133 model to adapt for the larger Knudsen number in the gas that may occur in the low ambient pressure

134 condition. The Knudsen number is defined as the ratio of the mean free path λ to a physical length

135 scale L: $Kn = \lambda/L$. Here, L can be a typical powder diameter in LPBF. The mean free path λ is

136 calculated as:

$$\lambda = \frac{\mu}{\rho}\sqrt{\frac{\pi}{2R_s T}} \tag{7}$$

137 In Eq. (7), μ is the gas viscosity, and R_S is the specific gas constant. The Knudsen number can be

138 used as the criterion to classify the "flow regimes" as follows [30, 31]:

139 • $0 \leq Kn \leq 0.01$: continuum flow (Navier-Stokes equation with no-slip boundary

140 condition).

141 • $0.01 \leq Kn \leq 0.1$: slip flow (Navier-Stokes equation with slip boundary condition).

142 • $Kn \gtrsim 0.2$: Navier-Stokes equation should be replaced with the Boltzmann equation

143 (statistical mechanics).

144 As will be presented later, the Knudsen number in the gaseous region is typically > 0.01 when the

145 ambient pressure is lower than 1 bar. Under this Knudsen number, the flow can enter the "slip

146 flow" regime, and the slip boundary condition needs to be applied. Under extremely low pressure,

147 the Knudsen number is > 0.2. This flow regime is beyond the capability of the current "continuum

148 flow" model described by Eqs. (1)-(4). Therefore, only ambient pressure larger than 10 mbar is

149 simulated (discussed later). The slip boundary condition can be written as:

$$V_{ct} - V_{gt} = \frac{2 - \sigma_v}{\sigma_v} \lambda \frac{\partial V_{gt}}{\partial n} \tag{8}$$

150   In Eq. (8), V_{ct} and V_{gt} are the tangential velocity on the condensed and gaseous side of the C-G

151   interface, and their difference is the velocity slip. σ_v is the tangential momentum accommodation

152   coefficient. $(\partial V_{gt}/\partial n)$ is the gradient of V_{gt} along the normal direction n of the C-G interface.

153   In the DEM computation, the initial powder bed configuration is randomly generated by a

154   rain-dropping algorithm [32]. Then, the motion of each powder particle is tracked according to the

155   Newton's equations of motion:

$$m_p \frac{d\vec{V}_{pc}}{dt} = \oint_{S_p} \vec{F}_f dS + m_p \vec{g} + \vec{F}_{col} \tag{9}$$

$$I_p \frac{d\vec{\omega}_p}{dt} = \oint_{S_p} \vec{r} \times \vec{F}_f dS \tag{10}$$

156   In Eqs. (9) and (10), m_p is the mass of the particle, $\vec{V}_{pc}$ is the velocity at the particle center, I_p is

157   the momentum of inertia of the particle, and $\vec{\omega}_p$ is the angular velocity of the particle. The

158   integrations on the right-hand-side of Eqs. (9) and (10) are carried out on the particle surface S_p.

159    $\vec{F}_f$ is the force exerted by the surrounding flow on S_p, which can be obtained from the CFD

160   computation. $\vec{r}$ is a vector pointing from the particle center to the particle surface. $\vec{F}_{col}$ is the force

161   resulted from the collision with surrounding particles. The force exerted on the ith particle by its

162   collision with the jth particle can be calculated as:

$$F_{col,ij} = -\left(\alpha_{k,ij}\delta_{ij} + \alpha_{d,ij}V_{n,ij}\right)n_{ij} \tag{11}$$

163   In Eq. (11), n_{ij} is a unit vector pointing from the ith particle to the jth particle. δ_{ij} is the gap between

164   the two particles calculated by $\delta_{ij} = R_i + R_j - d_{ij}$, where R_i and R_j are the radii of the ith and j^{th}

165   particles, and d_{ij} is the distance between the two particles. The collision force in Eq. (11) is only

166   activated when the gap δ_{ij} is negative, i.e., there is an overlap between the two particles. Otherwise,

167    $F_{col,ij}$ is set to be zero. $V_{n,ij}$ is the normal relative velocity of the ith particle with respect to the jth

168   particle, calculated as $V_{n,ij} = (V_i - V_j) \cdot n_{ij}$, where V_i and V_j are the velocities at the center of the

169   i^{th} and the jth particles. $\alpha_{k,ij}$ and $\alpha_{d,ij}$ are the spring and damping coefficient for the collision,

170   calculated by:

$$\alpha_{k,ij} = \left(\frac{8}{15}\right)^{0.8} \left[\left(\frac{R_i R_j}{R_i + R_j}\right)^2 \frac{m_i m_j}{m_i + m_j} \left(\frac{E}{1-v^2}\right)^4 v^2 \right]^{0.2} \tag{12}$$

$$\alpha_{d,ij} = 2m_i \zeta \sqrt{\frac{\alpha_{k,ij}}{m_i}} \tag{13}$$

171   In Eqs. (12) and (13), m_i and m_j are the mass of the ith and the jth particle. E is the Young's

172   modulus of the metal, v is the Poisson ratio, and ζ is the damping ratio.

173   In all the simulations and experiments of this work, the powder and substrate material is

174   stainless steel 316L, and the ambient gas material is argon. Their thermophysical properties used

175   in the CFD and DEM computation are listed in Table 1. The calculation domain and mesh of the

176   simulation are shown in Fig. 1. A fined mesh region (Fig. 1(a)) is defined to capture the major

177   physical phenomena, e.g., the molten pool dynamics and the powder-gas interaction. Coarse mesh

178   is extended from the fine mesh region along all ±X, ±Y, and ±Z directions, as shown in Fig. 1(b).

179   The purpose of the coarse mesh is to allow the gas flow to be fully developed within the calculation
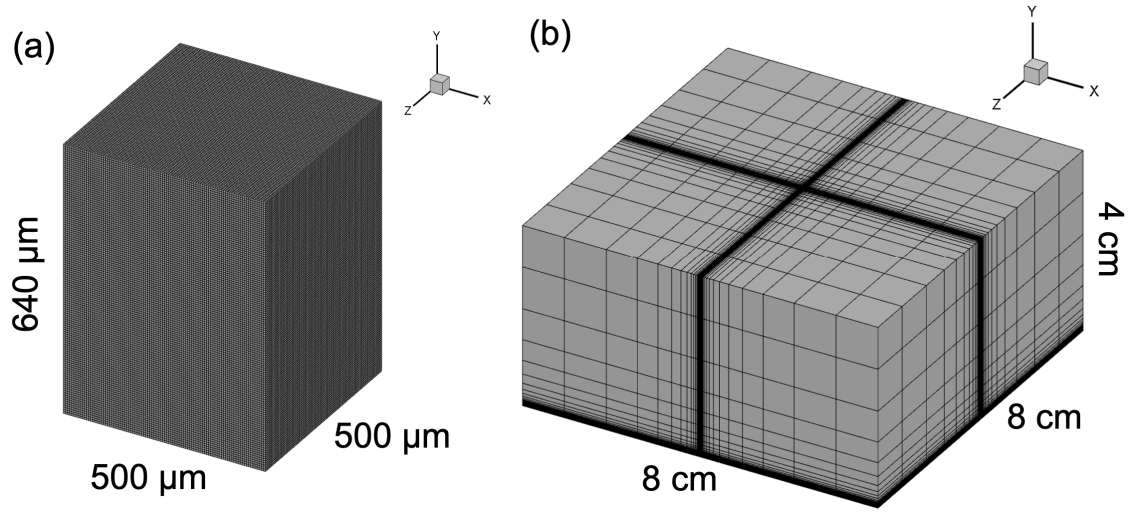
180   domain.

181

Fig. 1. Simulation domain and mesh. (a) Fine mesh region. (b) Entire calculation domain
184 **showing the coarse mesh extended from the fine mesh.**
185

186 *2.2 High-speed X-ray imaging*

187   High-speed synchrotron X-ray imaging experiment is performed for in-situ observation of the

188 powder motion during LPBF under various ambient pressure levels. The synchrotron X-ray beam

189 is provided by the 32-ID-B beamline of the Advanced Photon Source (APS), Argonne National

190 Laboratory (ANL). The detailed information about the setup for in-situ X-ray imaging of LPBF

191 has been documented in [12]. In brief, a miniature stainless steel 316L powder bed is assembled

192 with a metal plate (substrate) sandwiched by two glassy carbon plates, which are used to contain

193 the powder layer on top of the substrate. The powder layer is spread manually with 100 ± 10 μm

194 thickness. The width of the powder bed (the distance between two glassy carbon plates) is 500 μm.

195 **Table 1. Thermophysical properties of stainless steel 316 L and argon gas** [33-35]**.**

Property	Stainless Steel 316L			Argon
	Solid	Liquid	Vapor	
Density (kg m^{-3})	T dependent	T dependent	Ideal gas	Ideal gas
Phase change temperature (K)	1675 (solidus)	1708 (liquidus)	3135 (boiling)	--

11

Specific heat (J kg^{-1} K^{-1})	847	714	495	520
Phase change latent heat (J kg^{-1})	--	2.9×10^5 (melting)	7.45×10^6 (vaporization)	--
Thermal conductivity (W m^{-1} K^{-1})	T dependent	T dependent	T dependent	T dependent
Viscosity (kg m^{-1} s^{-1})	--	0.015	T dependent	T dependent
Surface tension (N m^{-1})	--	$1.7 - 1.5\times10^{-4}$ T	--	--
Young's Modulus (MPa)	2.2×10^3			
Poisson's ratio	0.3			
Damping ratio	0.5			
Tangential momentum accommodation coefficient				1.0

We note that a larger sample width will reduce the X-ray imaging visibility of the powder bed, while a smaller sample width makes the experiment deviate too much from a real LPBF process. The visibility of DZ is sacrificed in the current experiment, as a clear observation of DZ requires a much smaller sample width. A laser beam, with 1070 ± 10 nm wavelength and ~200 μm $1/e^2$ beam diameter, is used to melt the powder bed from above. The laser output is 312 W in power and 800 μs in duration in the present work. The laser beam is kept stationary to realize a "spot welding" type of laser melting. The powder particles have a mean diameter of 40 μm. The synchrotron X-ray beam penetrates and illuminates the laser-matter interaction region from the horizontal direction. The transmitted X-ray is converted into visible light by a LuAG:Ce scintillator, and then recorded by a high-speed visible-light camera (Photron FastCam SA-Z). The powder bed is enclosed in a vacuum chamber, refilled with high purity argon gas to adjust the inner chamber pressure.

3. Result and Discussion

Simulations and experiments are utilized simultaneously to investigate the effects of ambient pressure. Different ambient pressure levels are used in the investigation, as summarized in Table 2. Four ambient pressure levels in the atmospheric and sub-atmospheric (sub-atm) conditions (1 bar, 400 mbar, 50 mbar, 10 mbar) are investigated in both simulations and experiments. Hyper-atmospheric (hyper-atm) conditions are not investigated with experiments due to the difficulties of building a high-pressure chamber, but two hyper-atm pressure levels (3 bar, 5 bar) are investigated using simulations. Extremely low pressure levels (< 10 mbar) are not investigated in the current work because the Knudsen number is typically > 0.2, as discussed earlier. The current work will focus on the pressure range 10 mbar – 5 bar. For each pressure level in Table 2, at least three experiments and simulations are conducted with random initial configurations of the powder bed to ensure the statistical reliability of the results.

Table 2. Ambient pressure levels investigated.

Pressure group	Pressure Level	Investigation approach
Low pressure	10 mbar, 50 mbar	Experiment & Simulation
Medium pressure	400 mbar, 1 bar	Experiment & Simulation
High pressure	3 bar, 5 bar	Simulation

3.1 Overview of Simulation and Experimental Results

Exemplary results from the 3D simulation are shown in Fig. 2. The corresponding animations are given in Supplementary Video 1. A time sequence is presented in Fig. 2(a-e) to demonstrate the dynamic process. A variety of quantitative information, not directly measurable from the experiment, can be extracted from the simulation. Fig. 2(a, b) shows the laser absorption distribution and temperature field on the C-G interface. A vertical slice is extracted to show the

13

230   gas flow in Fig. 2 (c-e), where the temperature, velocity, (gauge) pressure, and vapor mass fraction

231   field can be quantified. The gauge pressure is defined as the difference between absolute and

232   ambient pressure, $p - p_{amb}$. The laser heating of the powder bed, shown by Fig. 2(a), results in the

233   powder melting, formation of the depression zone (DZ), and the powder motion (Fig. 2(b)). It can

234   be seen in Fig. 2(c, e) that the evaporation occurs at the molten pool surface, causing the formation

235   of the DZ and vapor jet. The vapor jet induces the entrainment of the surrounding gas, as shown

236   by the streamlines in Fig. 2(d). Both the vapor jet and the entrainment flow contribute to the

237   powder motion. These pieces of quantitative information will be examined thoroughly in later

238   discussions.
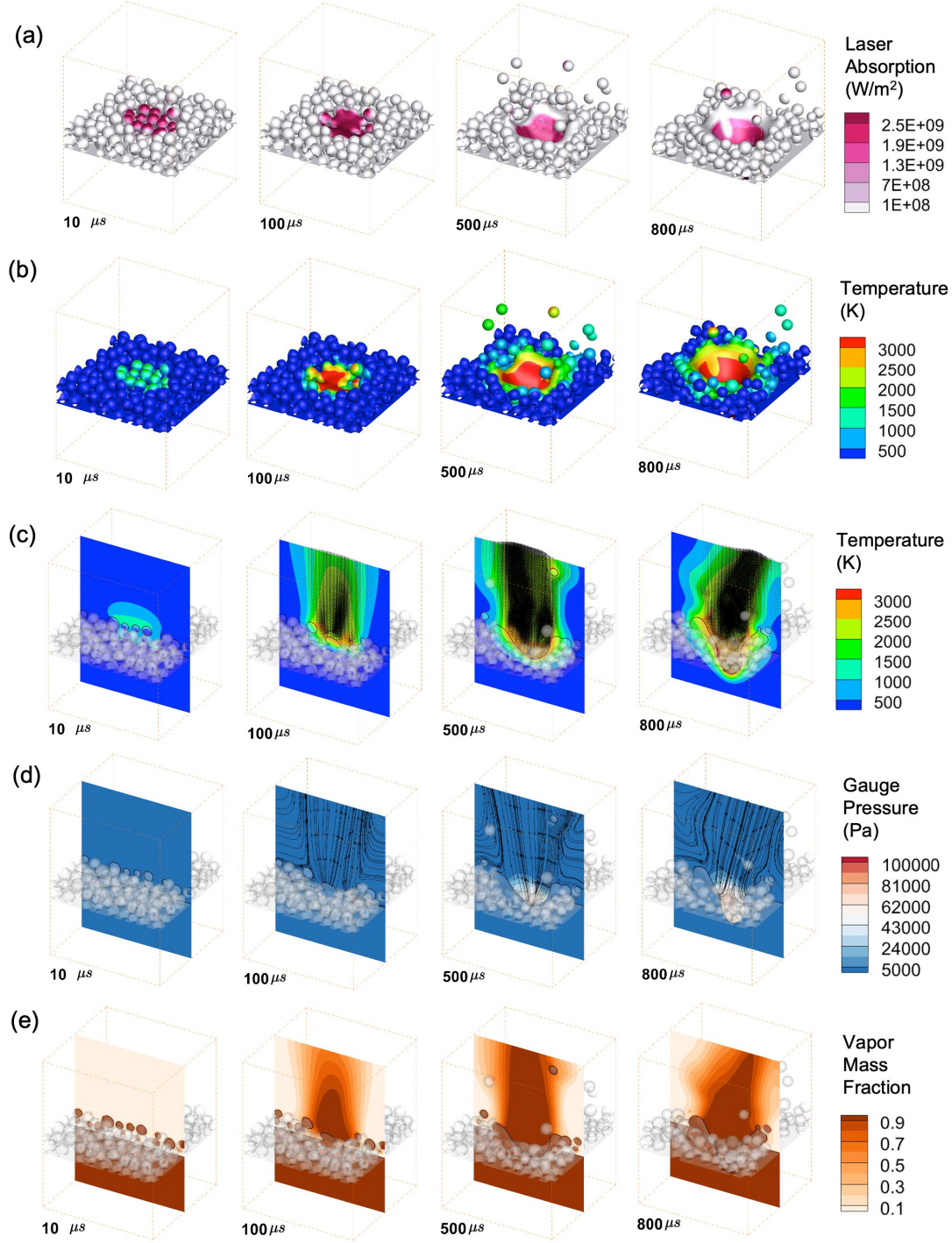
Fig. 2. Demonstration of the 3D model. A time sequence is selected from the simulation for p_{amb} = 400 mbar. The timestamp indicates the time period since the laser is turned on. (a) Laser absorption on the C-G interface. (b) The temperature on the C-G interface. (c) Vertical slice showing the temperature and flow field in the gaseous region. (d) Vertical slice showing the gauge pressure and streamlines of the flow in the gaseous region. (e) Vertical slice showing the vapor mass fraction field in the gaseous region.

247   To validate the current model, we compare between experiment and simulation results at the

248   pressure levels (1 bar, 50 mbar, 10 mbar) in Fig. 3(a-c). The animations for Fig. 3(a), Fig. 3(b),

249   and Fig. 3(c) are given as Supplementary Video 2, 3, and 4, respectively. As the ambient pressure

250   decreases, there are more spattered powder particles and the diverging angle of ejection increases.

251   These observations agree with the results in [12]. At each pressure level, we compared the velocity

252   of the ejected particles between experiment and simulation results, as shown in Fig. 4. Here, we

253   extracted the maximum velocity during the lifespan of each ejected particle and present the average

254   and extreme values over all the ejected particles with the error bars in Fig. 4. The magnitude of the

255   particle velocity matches reasonably well between simulation and experiment.

256   It is noticed that the ejected particles can be in a liquid form. These liquid particles can deform

257   and attach on other particles to form clusters, as seen in the X-ray imaging results in Fig. 3.

258   Unfortunately, the current model cannot capture the deformation and clustering of the liquid

259   particles. In the current model, the temperature distribution in the particle is calculated based on

260   the energy conservation (Eq. (3)). However, the fluid flow inside the particle is ignored, and the

261   particle is assumed to be a rigid body. Therefore, the particles in the current model cannot deform

262   or cluster with other particles (even if the temperature inside the particle is above the liquidus
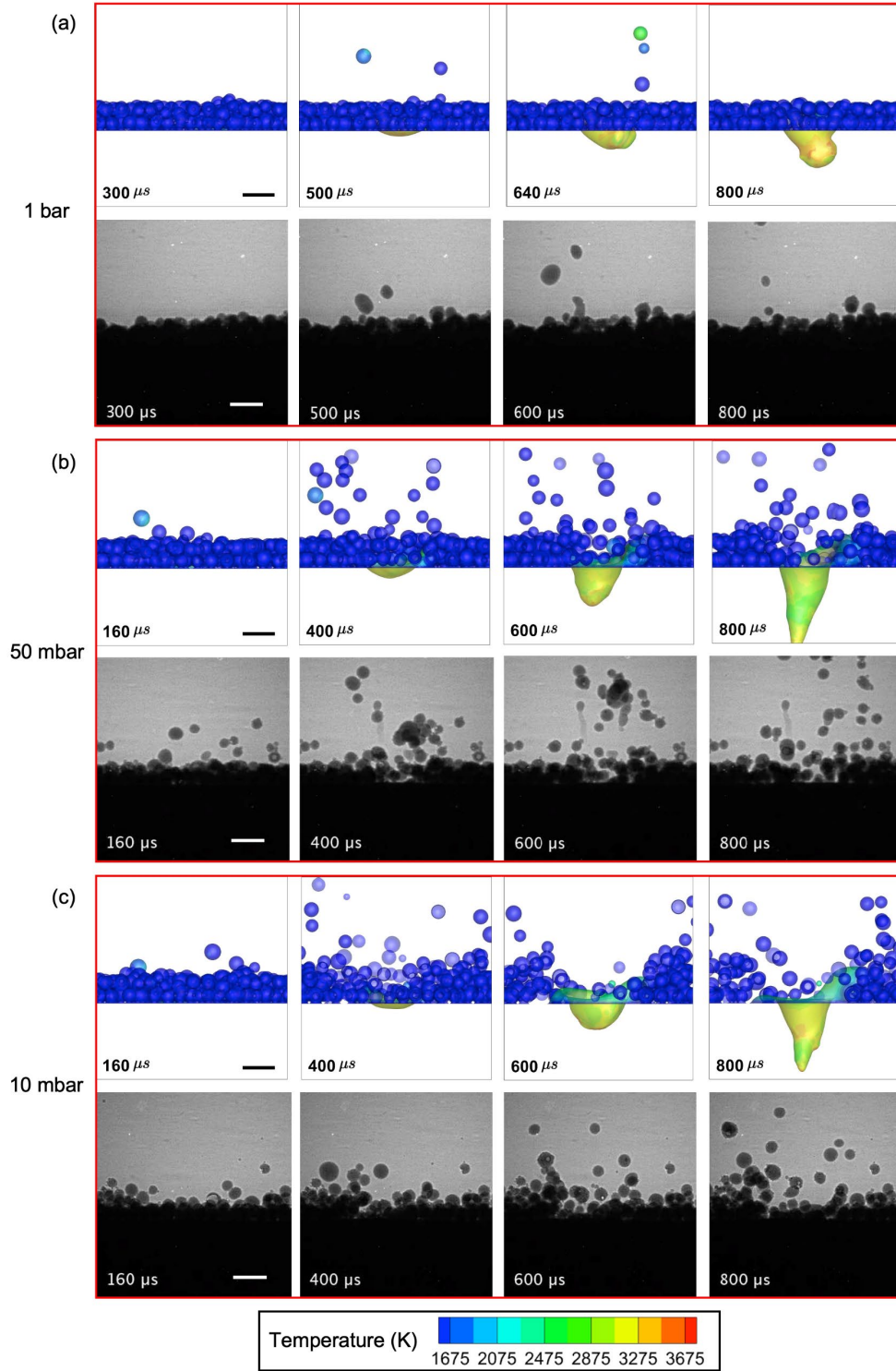
263   temperature).

264

265

Fig. 3. Powder motion from the simulation and X-ray imaging. (a) p_{amb} = 1 bar. (b) p_{amb} = 50 mbar. (c) p_{amb} = 10 mbar. The timestamp indicates the time period since the laser is turned on. All the scale bars are 100 μm. The simulation results are shown from a projected view similar to that in X-ray imaging experiments. The temperature is shown on the C-G interface for the simulation.
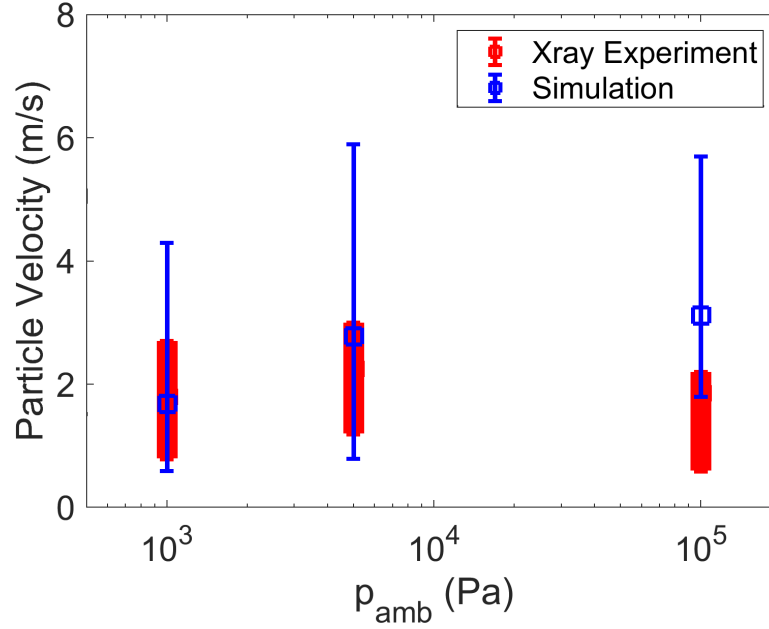
17

Fig. 4. Comparison of velocity for the ejected particles between X-ray experiment and simulation.

In the following discussion, the gas flow as a function of ambient pressure is first analyzed. After that, the powder motion driven by the powder-gas interaction are analyzed under different ambient pressure levels. Finally, we track the powder particles in all the simulations and statistically quantify the powder behavior, such as the velocity, forces, and temperature of the particles.

3.2 Vapor Jet and Induced Entrainment Flow

Significant gas flow occurs when the vapor jet initiates from the molten pool surface. The vapor jet then induces the entrainment of the ambient gas. The formation and development of the vapor jet at different ambient pressure levels are examined in Fig. 5. (5 bar, 1 bar, 10 mbar) are selected as the representative levels for the high-, medium-, and low-pressure groups in Table 2. In Fig. 5, a vertical slice with the temperature and flow field is extracted (as in Fig. 2(c)) at four moments to characterize the key physical events.
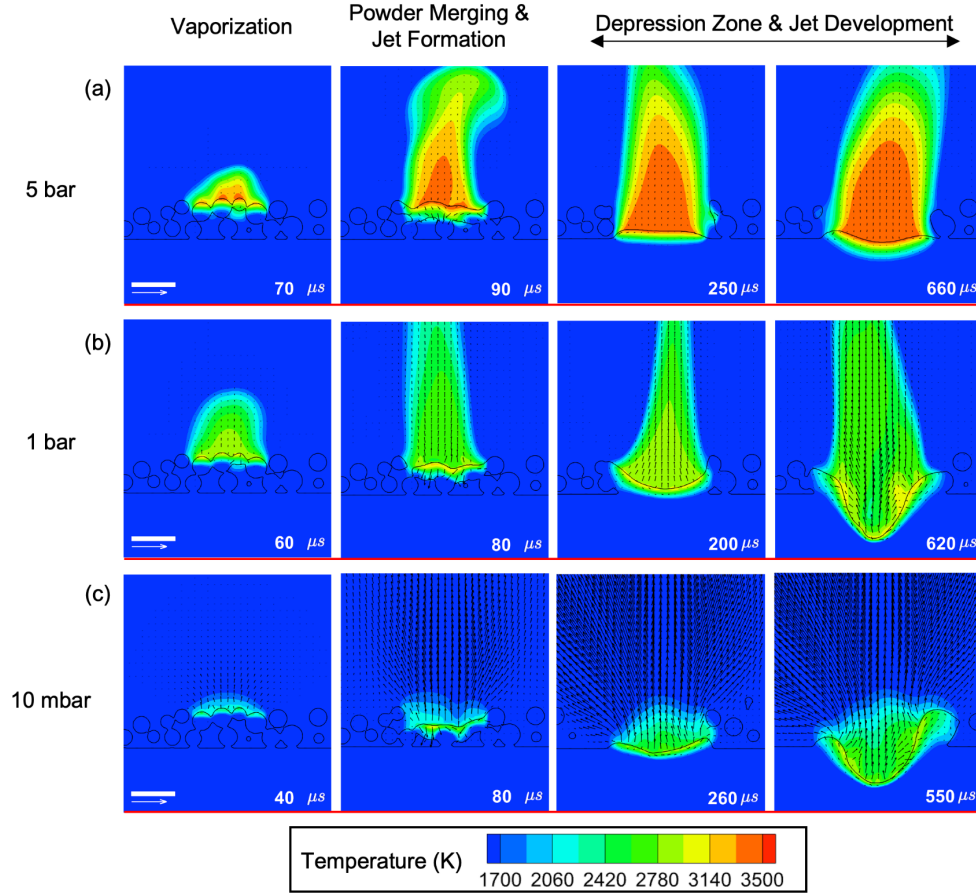
18

Fig. 5. Vapor jet formation and development under different ambient pressure levels. (a) p_{amb} = 5 bar. (b) p_{amb} = 1 bar. (c) p_{amb} = 10 mbar. For (a-c), a time sequence is given to characterize the key physical events. The vertical slice is at the same location shown in Fig. 2(c, d). All scale bars are 100 μm. All arrow keys are 2000 m/s in the gaseous region and 8 m/s for the condensed region.

It is observed in Fig. 5(a-c) that the evaporation initiates about 40 – 70 μs after the laser is turned on, which agrees with the observation in [12]. With the decrease of ambient pressure, the evaporation starts earlier because the boiling temperature is lower under lower pressure. According to the Clausius-Clapeyron equation, the boiling temperature is about 2350 K, 3150 K, and 3550 K under ambient pressure levels 10 mbar, 1 bar, and 5 bar, respectively. At about 80 – 90 μs, the powder particles merge into a molten pool, and a vapor jet emerges from the molten pool surface. After that, the vapor jet develops as the recoil pressure on the molten pool surface creates the DZ.

302   At the last moment in Fig. 5(a-c), the vapor jet has reached a "stable" state, where the temperature

303   and flow field do not significantly change with time.

304   Fig. 5 shows that the temperature in the vapor jet is significantly decreased as the ambient

305   pressure decreases. The stable vapor jet temperature at the opening of DZ is about 3400 K, 2700

306   K, and 2100 K, for p_{amb} = 5 bar, 1 bar, and 10 mbar, respectively. This can be again explained by

307   the lower boiling temperature under lower pressure. For the flow field, it can be observed that the

308   vapor jet is confined and has a small velocity under high ambient pressure (Fig. 5(a)). As the

309   ambient pressure decreases, the vapor jet expands more freely and has an increasingly larger

310   velocity (Fig. 5(b, c)).

311   To further analyze the structure of the vapor jet and induced entrainment flow, we extract

312   more quantitative information at the last moment in Fig. 5(a-c) when the vapor jet has reached the

313   stable state, as detailed in Fig. 6. The velocity magnitude in a vertical slice is shown in Fig. 6(a),

314   which is at the same slicing location as in Fig. 5. The pressure field and streamlines for the vertical

315   slice are shown in Fig. 6(b). To characterize the three-dimensional flow field, we extract a

316   horizontal slice cutting through the powder bed. The projected (horizontal) velocity magnitude is

317   shown in Fig. 6(c). The pressure field and streamlines for the horizontal slice is shown in Fig. 6(d).

318   The dashed circle in Fig. 6(c, d) marks the LIZ. We will use Fig. 6(a, b) to characterize the vapor

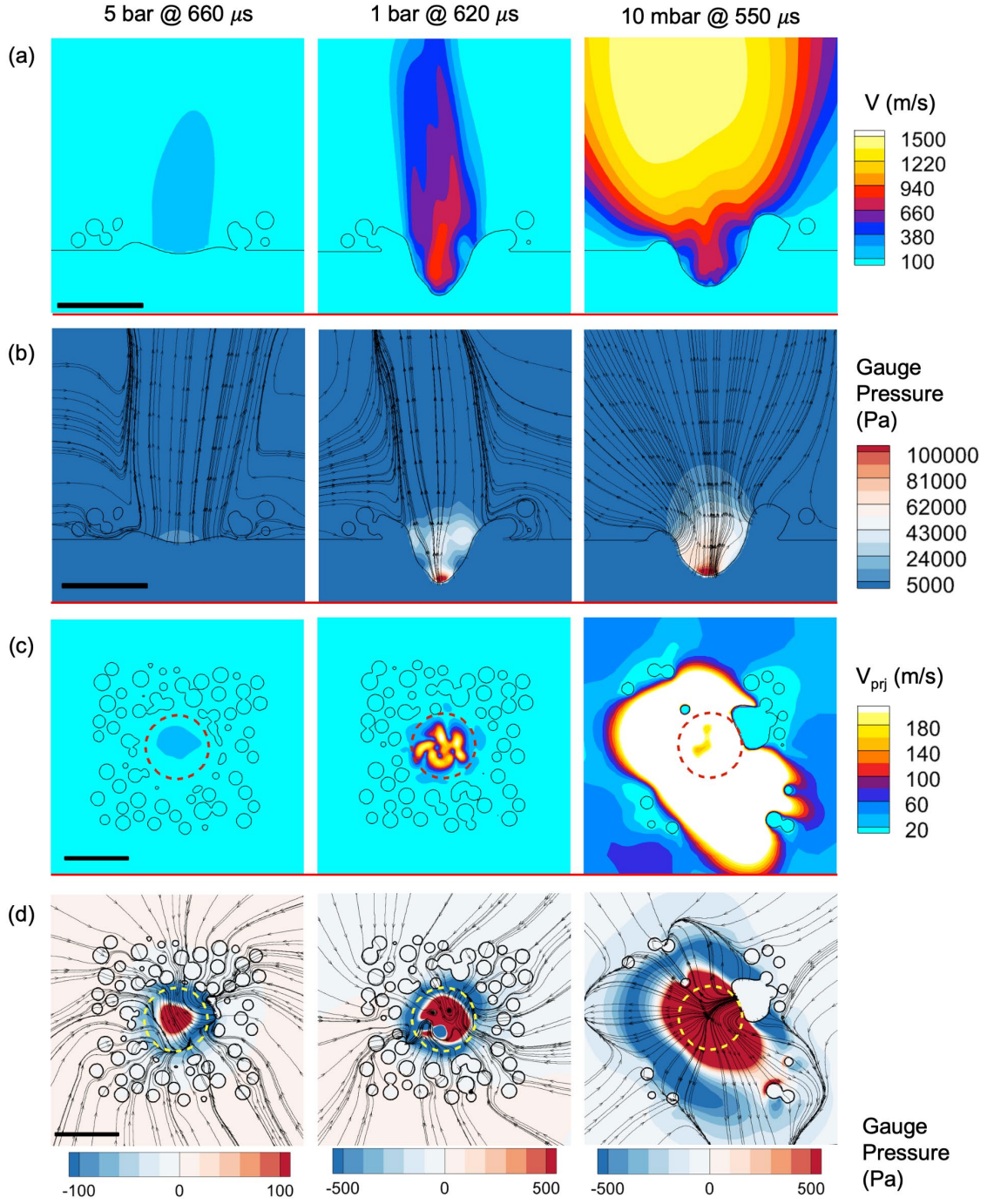319   jet expansion and Fig. 6(c, d) to characterize the induced entrainment flow.

Fig. 6. Gas flow structure at the stable state is analyzed for p_{amb} = 5 bar, 1 bar, and 10 mbar. (a) Velocity magnitude at a vertical slice. The slicing location is the same as that shown in Fig. 2(c, d) and Fig. 5. (b) Gauge pressure and streamlines at the same vertical slice. (c) Projected (horizontal) velocity magnitude at a horizontal slice cutting through the powder bed. (d) Gauge pressure and streamlines at the same horizontal slice. The red and yellow dashed circle in (c, d) indicates the LIZ. All the scale bars are 200 μm.

328   For all the ambient pressure levels, the vapor jet expansion is driven by the pressure decrease

329   from the DZ bottom towards the DZ opening, as shown in Fig. 6(b). The pressure decrease

330   corresponds to an increase of velocity magnitude from the DZ bottom towards the DZ opening

331   (Fig. 6(a)). The velocity reaches its maximum at a location above the DZ where the pressure does

332   not notably change anymore along the streamlines. Then, the velocity magnitude decreases radially

333   towards the ambient as the vapor jet momentum dissipates into its surrounding. We denote the

334   pressure difference between the DZ bottom and DZ opening in Fig. 6(b) as Δp_{exp}, which can be

335   viewed as the driving force for the vapor jet expansion. Δp_{exp} is relatively small ($\sim 10^4$ Pa) under

336   high ambient pressure (5 bar), which corresponds to a weak vapor jet expansion. Under 1 bar, Δp_{exp}

337   is increased to $\sim 10^5$ Pa. As the ambient pressure further decreases to 10^3 Pa, Δp_{exp} does not

338   significantly change, but the vapor jet expands with a larger diverging angle due to the less

339   confinement imposed by the small ambient pressure. The Bernoulli equation for the compressible

340   flow can be written as $\frac{1}{2}\rho v^2 + \frac{\gamma}{\gamma-1}p = $ constant, where ρ is the density, v is the streamline-wise

341   velocity, γ is the specific heat ratio, and p is the pressure. As the pressure decreases from the DZ

342   bottom to the DZ opening (by Δp_{exp}), the momentum ρv^2 increases according to the Bernoulli

343   equation. With the pressure decrease Δp_{exp} being similar ($\sim 10^5$ Pa) for the cases of $p_{amb} = 1$ bar

344   and $p_{amb} = 10$ mbar, the increase of momentum ρv^2 should also be comparable in these two cases.

345   Since ρ is significantly smaller for $p_{amb} = 10$ mbar, the velocity increase is significantly larger. To

346   summarize, the vapor jet velocity is expected to increase as the ambient pressure decreases, which

347   is confirmed in Fig. 6(a). The vapor jet expansion velocity, V_{exp}, can be characterized by the

348   maximum velocity in the vapor jet. V_{exp} is plotted as a function of p_{amb} in Fig. 5(a) where V_{exp} is

349   about 200 m/s, 1000 m/s, and 1500 m/s for $p_{amb} = 5$ bar (5×10^5 Pa), 1 bar (1×10^5 Pa), and 10 mbar

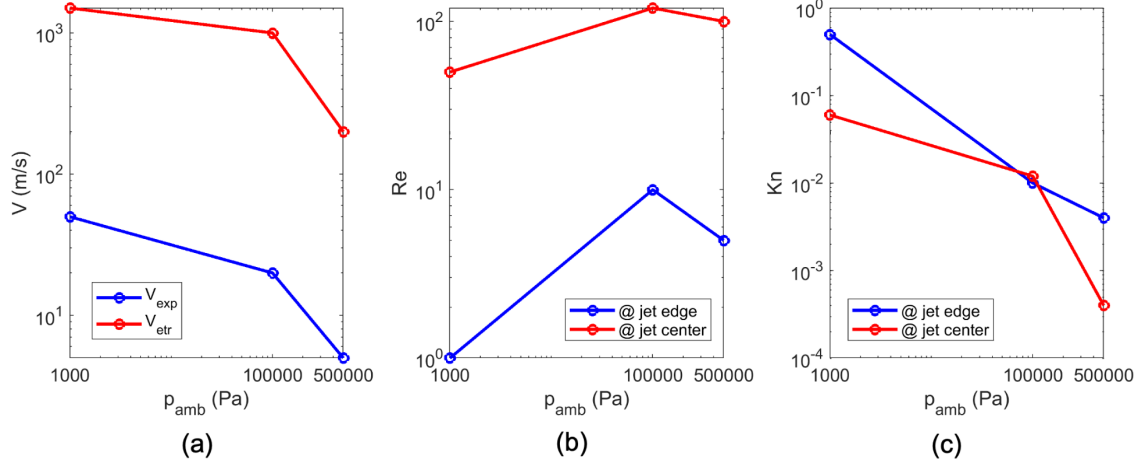350   (1×10^3 Pa), respectively.

Fig. 7. Gas flow characteristics as a function of ambient pressure. (a) Characteristic vapor jet expansion velocity V_{exp} and induced entrainment velocity V_{etr}. (b) Reynolds number at the jet center and jet edge. (c) Knudsen number at the jet center and jet edge. All the quantities are extracted based on the vertical and horizontal slices shown in Fig. 6.

The induced entrainment flow is visualized by the streamlines in Fig. 6(d). For all ambient pressure levels, a high-pressure region is formed in the LIZ (dashed circle), where the vapor jet is initiated. Right outside the high-pressure region, there is a "ring" of low-pressure region beyond which the pressure is close to the ambient pressure. The low-pressure ring acts as a separation between the entrained gas and the expanding vapor. Outside the "ring," the gas is driven towards the LIZ by the pressure difference between the "ring" and ambient. Inside the ring, the gas radially expands from the LIZ outwards. We denote the pressure difference between the ambient and the low-pressure ring as Δp_{etr}, which can be viewed as the driving force for the entrainment flow. Δp_{etr} is relatively small (~ 100 Pa) under high ambient pressure (5 bar), indicating weak entrainment. At 1 bar, Δp_{etr} is increased to ~ 500 Pa. Δp_{etr} does not significantly change as the ambient pressure further decreases to 10 mbar, but the size of the low-pressure ring is significantly increased due to the enhanced vapor jet expansion. Again, according to the Bernoulli equation, Δp_{etr} can cause larger entrainment velocity under low ambient pressure. As confirmed in Fig. 6(c), the entrainment velocity is increased as the ambient pressure decreases. The entrainment velocity, V_{etr}, can be

23

371 characterized by the projected velocity at the outer edge of the low-pressure ring. V_{etr} is plotted as

372 a function of p_{amb} in Fig. 5(a) where V_{etr} is ~ 5 m/s, 20 m/s, and 50 m/s for $p_{amb} = 5$ bar (5×10^5 Pa),

373 1 bar (1×10^5 Pa), and 10 mbar (1×10^3 Pa), respectively.

374   Finally, we quantify the Reynolds number (Re) and Knudsen number (Kn) for the gas flow as

375 functions of ambient pressure, as shown in Fig. 7(b, c). The Reynolds number is defined as $Re =$

376 $\rho U L / \mu$, where ρ is the gas density, U is the velocity magnitude, μ is the gas viscosity, and L is a

377 physical length scale chosen to be 50 μm as the typical diameter of a large powder particle. The

378 Knudsen number is again defined as $Kn = \lambda / L$. The Reynolds number is considered as the ratio

379 between the inertia and viscous force and has been used to estimate the drag force exerted by the

380 gas flow on powder particles [1, 25]. The Knudsen number, as discussed earlier, can be used to

381 judge whether statistical mechanics or (continuum) fluid dynamics governs the flow behavior. We

382 select two locations in the horizontal slice in Fig. 6(c, d) to characterize Re and Kn of the gas flow.

383 The first location is the center of the LIZ, which is considered the typical location where the

384 powder particles are ejected. The second location is a typical location on the outer edge of the low-

385 pressure ring, where powder particles are subjected to the entrainment flow. These two locations

386 are denoted as "jet center" and "jet edge," and their (Re, Kn) values are calculated from simulations

387 and shown in Fig. 7(b, c).

388   It is observed in Fig. 7(b) that the Reynolds number does not vary notably for the high and

389 medium pressure levels (5 bar and 1 bar). Re is ~ 100 at the jet center and ~ 10 at the jet edge.

390 Under low ambient pressure (10 mbar), Re decreases to ~ 50 at the jet center and ~ 1 at the jet

391 edge. The decrease of Re can be attributed to the small gas density due to the low ambient pressure.

392 It is also noted that the Reynolds number is typically 1 – 2 magnitudes smaller at the jet edge than

393 the jet center. The drag force on powder particles can be estimated using the "Stokes limit"

394   assumption [1], which assumes that the Reynolds number approaches zero. We point out that the

395   Stokes limit assumption can be justified for the entrainment flow around the powder particles as

396   Re $\leq$ 10. However, the Reynolds number is ~ 100 for the surrounding gas flow when powder

397   particles are ejected. In such a case, the Stokes limit assumption should be applied with caution.

398   It can be observed in Fig. 7(c) that the Knudsen number increases remarkably as the ambient

399   pressure decreases. It is safe to assume that a continuum gas flow for high ambient pressure (5

400   bar), as Kn is 0.0004 – 0.004. The Knudsen number for the medium pressure (1 bar) is about 0.01,

401   indicating the necessity of employing the slip boundary conditions even at the atmospheric

402   pressure. The no-slip boundary condition should be carefully employed in gas flow simulations

403   for LPBF, and it should be replaced by the slip boundary condition when Kn > 0.01. Under low

404   ambient pressure (10 mbar), Kn is 0.05 – 0.5, which suggests that the continuum flow assumption

405   will be invalid should the ambient pressure be further decreased. We stress that caution needs to

406   be exercised when carrying out continuum fluid dynamics simulations under extremely low

407   ambient pressure levels for LPBF.

408

409   *3.3 Powder Motion Driven by Powder-Gas Interaction*

410   The vapor jet and induced entrainment flow determine the powder-gas interaction, which

411   drives the powder motion. The typical powder particle trajectories at 1 bar are shown in Fig. 8. An

412   isometric view is given in Fig. 8(a), where five typical particle trajectories are shown in lines with

413   circle markers (the triangle markers indicate the initial location). The red cylinder indicates the

414   laser, and the box in light blue indicates the powder bed. The Y direction is the vertical direction,

415   and (X, Z) are the two horizontal directions. Fig. 8(b-d) shows three projection views from the X-

416   Z, X-Y, and Z-Y plane.

417   These results confirmed the four characteristic models of powder-gas interaction that we

418   identified with our previous 2D model. The four modes are briefly introduced below, with more

419   details given in [26]:

420   • Recoil mode: It is defined when significant evaporation occurs on the surface of the powder

421   particle, and the recoil pressure dominates over the drag force (gas-flow-induced force) on the

422   particle surface. The powder particle is driven toward the opposite direction of the vapor jet by

423   the recoil pressure.

424   • Entrainment mode: It is defined when the surroundings of the particle are dominated by the

425   entrainment flow, and the particle is driven by the drag force towards the LIZ.

426   • Elevation mode: It is defined when the particle is simultaneously subject to the entrainment

427   flow and the vapor jet expansion, and the particle is vertically ejected by the drag force with a

428   relatively small divergence angle.

429   • Expulsion mode: It is defined when the surroundings of the particle are dominated by the

430   expanding vapor jet, and the particle is ejected by the drag force with a relatively large

431   divergence angle.

432   The powder motion can be governed by one powder-gas interaction mode or a sequence of modes.

433   Specifically, for the simulation result in Fig. 8, Particles 1 and 5 are sequentially governed by the

434   entrainment, elevation, and expulsion mode. They are entrained towards and subsequently ejected

435   from the LIZ. Particle 2 is dominated by the elevation mode. It moves vertically upwards with

436   neither entrainment nor ejection. Particle 3 is dominated by the expulsion mode. It is ejected by a

437   tilted vapor jet with a large divergence angle. Particle 4 sequentially experiences the entrainment,

438   elevation, and recoil mode. It is first entrained into the LIZ, and then evaporation occurs on its top

26

439   surface due to laser heating. Finally, the recoil mode drives the particle to dive into the molten

440   pool.
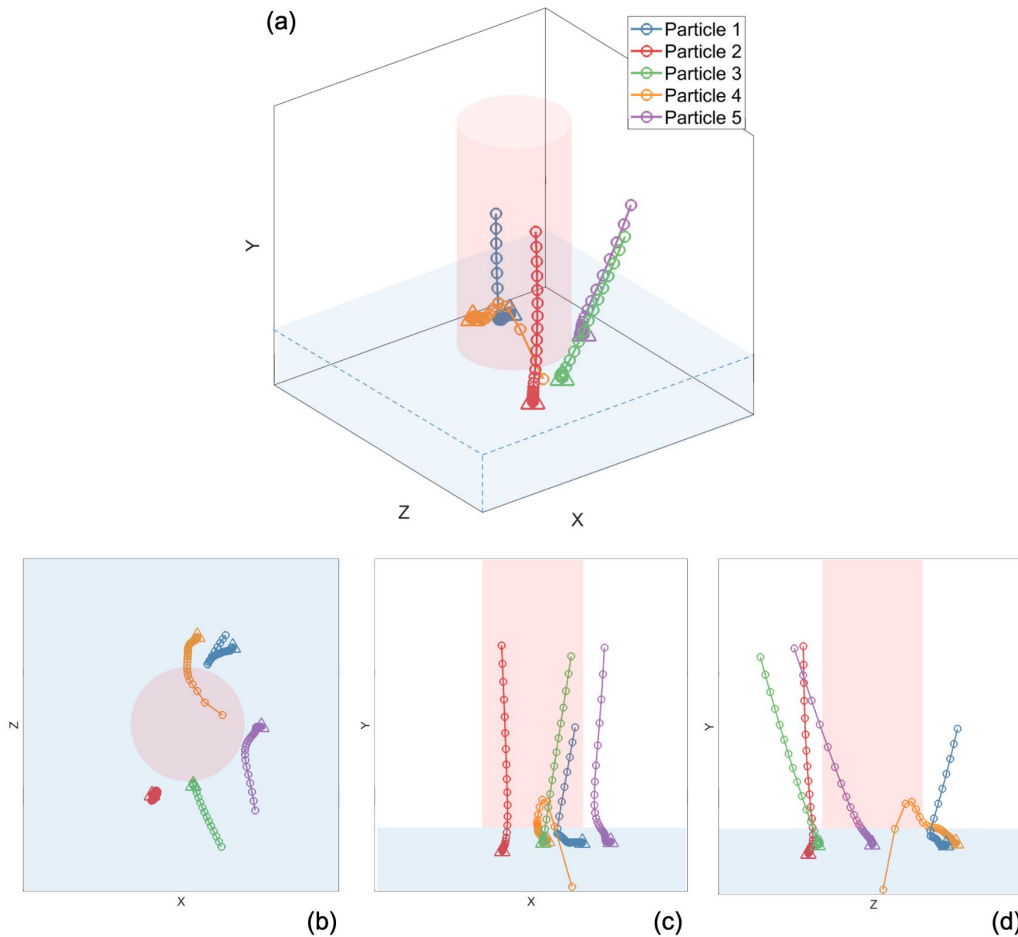
442   **Fig. 8. Typical particle trajectories at 1 bar (atmospheric pressure).** (a) Isometric view where
443   the particle trajectories are lines with circle markers. The triangle marker indicates the initial
444   locations of the particles. The red cylinder indicates the laser. The box in light blue indicates the
445   powder bed. The Y direction is the horizontal direction, and (X, Z) are the two vertical directions.
446   (b-d) Projected views of (a) from X-Z, X-Y, and Y-Z plane.

447

448   A new powder ejection mechanism, denoted as the "recoil-mode" powder ejection, is

449   identified in the current simulations. Two typical powder particles governed by the recoil mode

450   ejection are shown as Particles 6 and 7 in Fig. 9. Again, an isometric view is given in Fig. 9(a),

451   and three projection views from the X-Z, X-Y, and Y-Z plane are given in Fig. 9(b-d). Particles 6

452   and 7 are first entrained and then ejected at a large ejecting angle (for Particle 7), or even

453   downwards to the powder bed (for Particle 7). To quantify the transient situation for Particle 6,

454   vertical planes can be determined by the laser centerline and the center of Particle 6 at selected

455   moments, and the temperature and flow field on the planes are shown in Fig. 10. The entrainment-

456   ejection particle motion can be observed in Fig. 10(a) where Particle 6 is circled in red. Although

457   the entrainment-ejection motion is similar to Particles 1 and 5 in Fig. 8, the driving force for the

458   ejection is different. The temperature and flow field surrounding Particle 6 is zoomed in at two

459   key moments (450 μs and 530 μs), as shown in Fig. 10(b, c). At 450 μs, the upper left corner of

460   Particle 6 cuts into the LIZ, and the laser heating causes significant local evaporation. As a result,

461   the recoil pressure pushes the particle away from the LIZ and downwards to the powder bed. At

462   530 μs, Particle 6 has departed from the LIZ but is heated at the lower left corner by the reflected

463   laser beam. The reflected beam can be traced back to the asymmetric DZ clearly seen in Fig. 10(a).

464   Therefore, Particle 6 is again subject to recoil pressure, and the latter subsequently ejects Particle

465   6 at a large ejecting angle. Particle 7 also cuts into the LIZ (Fig. 9(b)) when it is heated by the laser

466   on its top (similar to the scenario in Fig. 10(b)). But Particle 7 is not subsequently heated by the

467   reflected laser at its bottom position. Therefore, recoil pressure is only generated on the top of the

468   particle to push it downwards to the powder bed. It is noted that the recoil-mode powder ejection

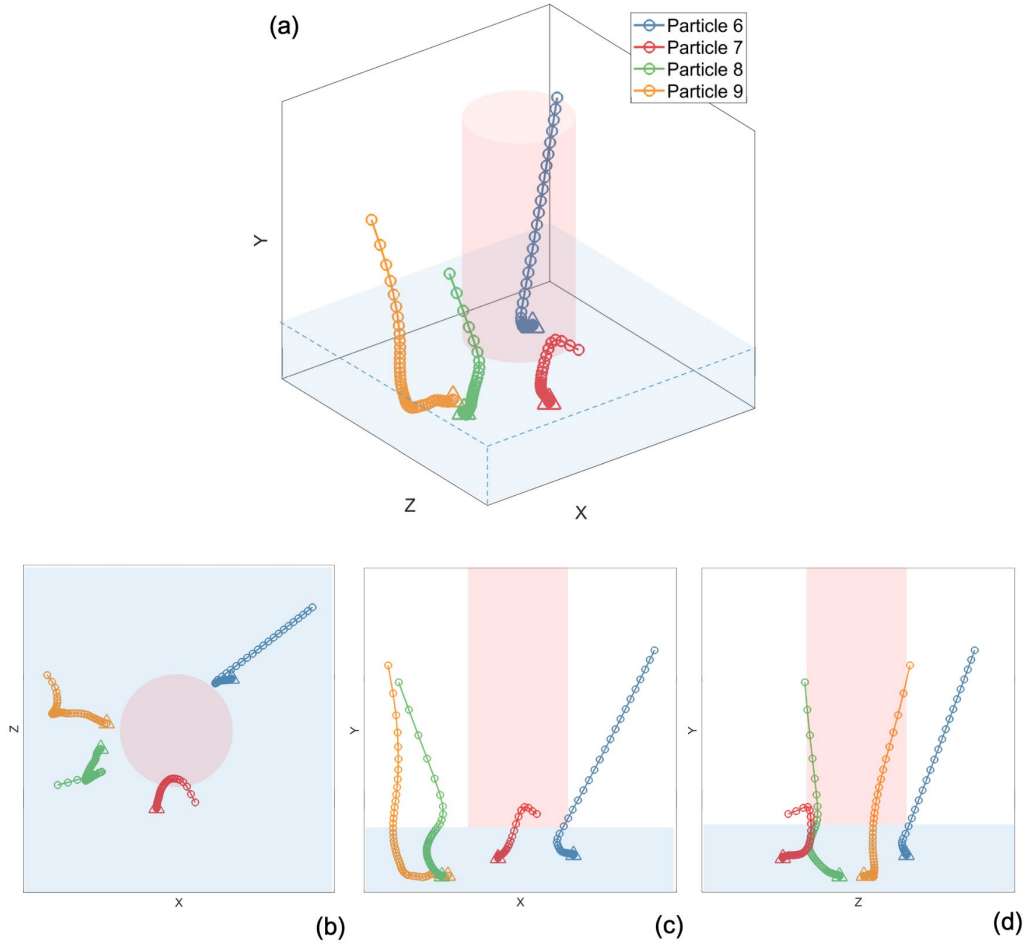469   is also inferred from experimental observations [1, 5].

Fig. 9. Miscellaneous powder particle trajectories. Particle 6 is under p_{amb} = 3 bar. Particle 7 is under p_{amb} = 5 bar. Particles 8 and 9 are under p_{amb} = 50 mbar. (a) Isometric view where the powder trajectories are lines with circle markers. The triangle marker indicates the initial locations of powder particles. The red cylinder indicates the laser. The box in light blue indicates the powder bed. The Y direction is the horizontal direction, and (X, Z) are the two vertical directions. (b-d) Projected views of (a) from X-Z, X-Y, and Y-Z plane.

The recoil-mode powder ejection is found to be active only in the cases with medium- and high-pressure groups in Table 2. In the cases of medium pressure, the contribution of the recoil mode to the powder ejection is minor, and the powder ejection is primarily driven by the expulsion mode, where the expanding vapor jet exerts drag force on and ejects the powder particles. In the high-pressure conditions, the drag force becomes significantly smaller due to the reduced vapor jet velocity (Fig. 6). The expulsion mode weakens, and the recoil mode becomes the dominating mechanism for the powder ejection. As a result, the recoil-mode ejection is mostly distinguishable

485   in the high-pressure simulations. As for the low-pressure cases, no recoil-mode ejection can be

486   identified because the powder particles are typically ejected by the enhanced vapor jet expansion

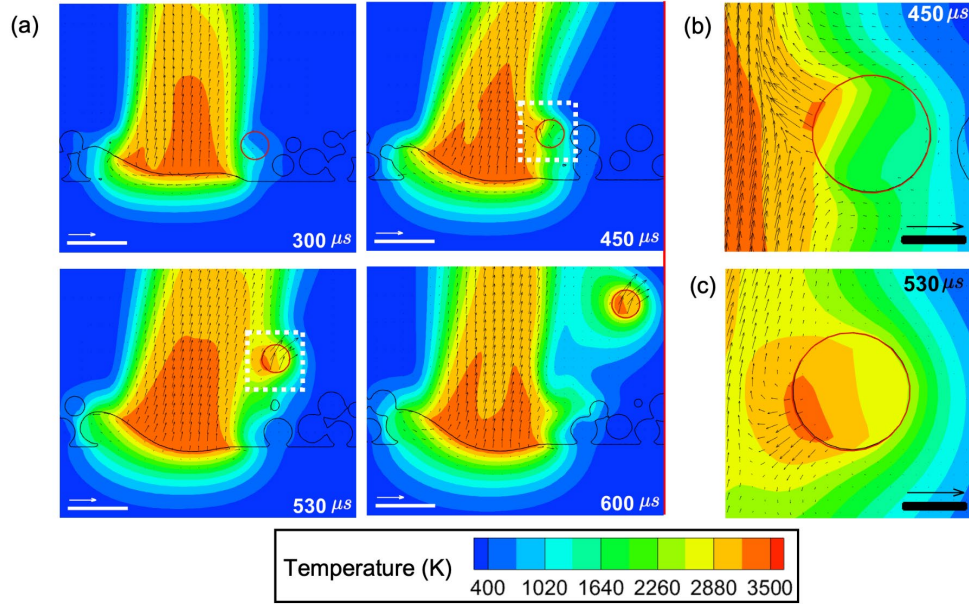487   before they can be significantly heated by the laser.

Fig. 10. Recoil-mode ejection under p_{amb} = 3 bar. (a) Time sequence from a vertical slice formed by the laser centerline and the center of Particle 6 (red-circled). The slice shows the temperature and flow field. The scale bars are 100 μm. The arrow keys are 500 m/s for the gaseous region and 2 m/s for the condensed region. (b, c) The temperature and flow field surrounding Particle 6 is zoomed in at 450 μs and 530 μs. The scale bars are 25 μm. The arrow keys are 250 m/s for the gaseous region. The flow field inside the particle is not shown.

496   Two new sequences of powder-gas interaction modes have also been identified that can cause

497   complicated powder motions, as demonstrated by Particles 8 and 9 in Fig. 9. Fig. 9(c) shows a

498   meandering trajectory for Particle 8: it is first ejected, then entrained, and finally ejected again.

499   Particle 8 can be considered sequentially governed by the expulsion mode, entrainment mode, and

500   again expulsion mode, which suggests a competition between the vapor jet expansion and the

501   entrainment flow surrounding Particle 8. To visualize the competition, we extract the horizontal

502   slices cutting through the center of Particle 8 at four moments, as shown in Fig. 11(a). As Particle

503   8 is elevating during this meandering motion, the slicing locations for the four moments in Fig.

504   11(a) are Y = 28.5 μm, 56.8 μm, 90.7 μm, and 150.5 μm, respectively, with Y = 0 being the

505   substrate surface location. At 230 μs in Fig. 11(a), Particle 8 (solid red circle) is ejected from the

506   LIZ (dashed red circle) by the expanding vapor jet, governed by the expulsion mode. At 420 – 580

507   μs, Particle 8 is away from the vapor jet expansion, and its surroundings are dominated by the

508   entrainment flow, as shown by the zoomed-in flow field in Fig. 11(b, c). Therefore, Particle 8 is

509   governed by the entrainment mode and is driven towards the LIZ. Finally, Particle 8 meets the

510   expanding vapor jet again at 680 μs. Following this, Particle 8 is again governed by the expulsion

511   mode and is ejected from the LIZ. It is noted that the ejection-entrainment motion of Particle 8 has
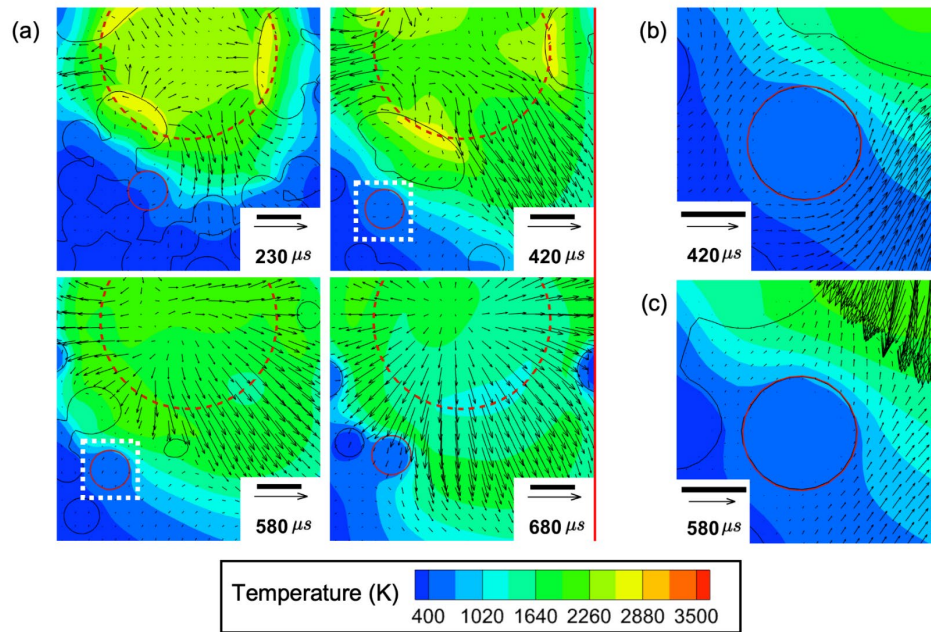
512   also been observed in the experiments [12].

514   **Fig. 11. Meandering powder motion under p_{amb} = 5000 mbar.** (a) Time sequence from a
515   horizontal slice cutting through the center of Particle 8 (solid circle in red). The slices show the
516   temperature and flow field. The red-dashed circle indicates the laser diameter (LIZ). The scale bars
517   are 50 μm. The arrow keys are 1000 m/s for the gaseous region and 4 m/s for the condensed region.
518   (b, c) The temperature and flow field surrounding Particle 8 is zoomed in at 420 μs and 580 μs.
519   The scale bars are 25 μm. The arrow keys are 50 m/s for the gaseous region. The flow field inside
520   the particle is not shown.
521

522   The second new sequence of powder-gas interaction modes manifests in Particle 9 (Fig. 9),

523   which is sequentially governed by the ejection and elevation mode. There is a similar competition

524   between the vapor jet expansion and the entrainment flow surrounding Particle 9. As can be seen

525   in Fig. 9(c), Particle 9 is first ejected from the LIZ governed by the expulsion mode. As Particle 9

526   moves away from the LIZ, the vapor jet expansion weakens while the entrainment flow is

527   strengthened. As the effects of these two flows are balanced, Particle 9 is governed by the elevation

528   mode, which drives Particle 9 to move vertically upwards (Fig. 9(c, d)) with little horizontal

529   movement (Fig. 9(b)).

530   As exemplified by Particles 8 and 9, the particles can be governed by new sequences of

531   powder-gas interaction modes following their initial ejection from the LIZ, which leads to their

532   complex motions. These new sequences of powder-gas interaction modes are caused by the

533   balance (or imbalance) between the two driving forces stemming from the vapor jet expansion and

534   the entrainment flow. It is noted that these sequences of modes and the consequent powder motions

535   are almost exclusively observed in the low-pressure group (Table 2). This can be explained by the

536   wide low-pressure ring observed under low ambient pressure (Fig. 6(d)), which creates more

537   opportunities for the entrainment flow to balance or even overcome the vapor jet expansion,

538   resulting in the new mode sequences and the complex powder motions. In contrast, the low-

539   pressure ring observed for higher ambient pressure levels is narrow (Fig. 6(d)). Therefore, once

540   the ejected powder particles pass the low-pressure ring, the weak entrainment flow is not adequate

541   to alter the particle trajectory.

542

543   *3.4 Statistical Quantification of Powder Behavior*

544   We have repeated the simulation four times at each ambient pressure level in Table 2 with

545   random initial powder bed configurations. For each simulation, quantities such as velocity and

546   average temperature can be tracked for each powder particle (examples are given in Appendix A).

547   Statistical quantification is carried out to show the powder-related quantities as functions of

548   ambient pressure, as shown in Fig. 12. The detailed definitions of the terms in Fig. 12 and the

549   methods of extracting the values for these terms are given in Appendix B.
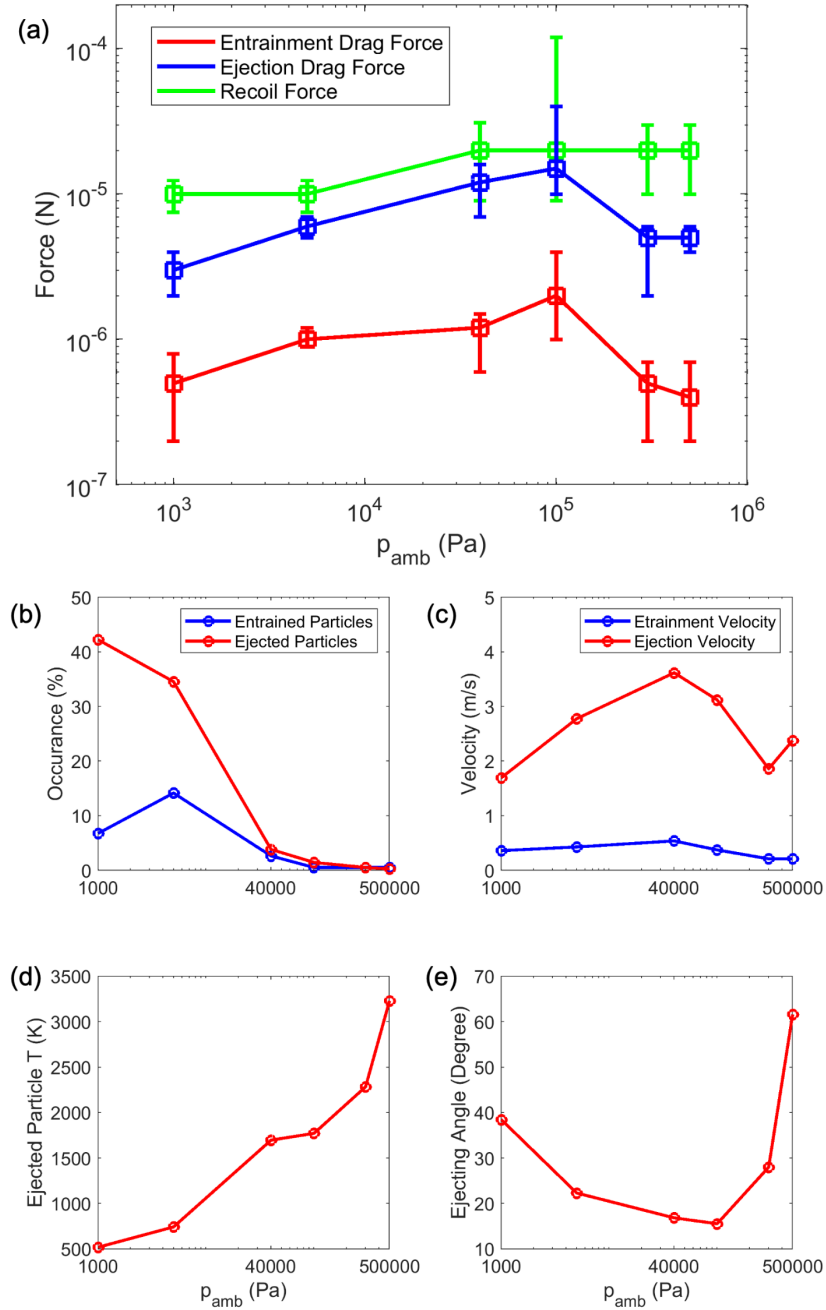
Fig. 12. Statistical quantification of powder behavior as a function of the ambient pressure. The definitions of the terms in (a-e) and the method of extracting these pieces of information are detailed in Appendix B. (a) Magnitudes of the entrainment drag, ejection drag, and recoil forces. (b) Occurrences of the entrained and ejected particles. (c) Entrainment and ejection velocities. (d) The temperature of the ejected particles. (e) The ejecting angle of the ejected particles.

In Fig. 12(a), the magnitudes of the drag and recoil forces (defined in Appendix B) on powder

particles are shown as functions of the ambient pressure. The drag forces (both for powder

34

559 entrainment and ejection) are the maximum at the medium-pressure levels. In the cases of the high-

560 pressure levels, the drag forces are reduced because the gas flow velocity (both vapor jet expansion

561 and induced entrainment flow) is small, as shown in Fig. 6(a, c). In the cases of the low-pressure

562 levels, although the gas flow velocity is increased, the flow enters the "slip flow" regime, and the

563 drag force decreases with the increasing Knudsen number [30]. The ejection drag force (10^{-6} – 10^{-5}

564 ^{5} N) is typically one magnitude larger than the entrainment drag force (10^{-7} – 10^{-6} N) for all ambient

565 pressure levels. The recoil force, in most cases, only briefly occurs on the top surface of powder

566 particles when the vapor jet begins to form. The particles subject to the recoil force then rapidly

567 merge into the molten pool. In this scenario, the magnitude of recoil force (10^{-5} N) does not

568 significantly change with the ambient pressure. At medium and high ambient pressure levels,

569 however, a few particles can have a larger recoil force (up to ~ 10^{-4} N) when they are ejected (e.g.,

570 Particles 6 and 7 in Fig. 9) or dives into the molten pool (e.g., Particle 2 in Fig. 8) driven by the

571 recoil mode. This explains the larger error bar for medium and high ambient pressure levels in Fig.

572 12(a).

573   Next, the occurrences of entrained and ejected particles (defined in Appendix B) are counted

574 in Fig. 12(b) as functions of the ambient pressure. It is observed that the occurrence of ejected

575 particles increases with decreasing ambient pressure, which is due to the enhanced vapor jet

576 expansion. The occurrence of entrained particles first increases with decreasing ambient pressure

577 but decreases at the lowest pressure level (10 mbar, i.e., 10^3 Pa). The increase of entrained particles

578 can be attributed to the wider low-pressure ring under lower ambient pressure (Fig. 6(d)). However,

579 the entrainment drag is reduced significantly at the lowest pressure level, as discussed in Fig. 12(a),

580 which explains the decrease of entrained particles.

581   The entrainment and ejection particle velocity (defined in Appendix B) are plotted as

582   functions of the ambient pressure in Fig. 12(c). The particle velocities are the maximum at the

583   medium pressure levels and decrease for lower or higher pressure levels, which is consistent with

584   the trend for the entrainment and ejection drags in Fig. 12(a). For high ambient pressure levels, the

585   ejection velocity is typically smaller due to the smaller ejection drag. However, when the recoil-

586   mode ejection occurs, the ejection velocity can be large despite the smaller drag force. Therefore,

587   there is an increase in ejection velocity for the highest pressure level (5 bar, or 5×10^5 Pa).

588   It is noticed in Fig. 12(c) that the entrainment velocity ($\sim$ 0.5 m/s) is typically smaller than the

589   ejection velocity ($\sim$ 3 m/s). The velocity magnitude can only be qualitatively compared with X-

590   ray imaging results, as the particle velocity observed in X-ray imaging is only the projected

591   velocity. Typical particle trajectories are manually extracted from the X-ray imaging to calculated

592   the projected particle velocity (examples given in Appendix A). The measured maximum velocity

593   in a particle's lifespan agrees with the range 0.5 – 3 m/s in Fig. 12(c).

594   Finally, the temperature and ejecting angle (defined in Appendix B) of the ejected particles

595   are quantified as functions of the ambient pressure, as shown in Fig. 12(d, e). As can be seen in

596   Fig. 12(d), the temperature of the ejected particles increases from 500 K to almost 3500 K as the

597   ambient pressure increases from 10 mbar (1×10^3 Pa) to 5 bar (5×10^5 Pa). This trend agrees with

598   the observation in [14] and can be explained as follows. Under high ambient pressure, the boiling

599   temperature of the metal is increased, and therefore, the powder particles can be further heated

600   before being ejected by the vapor jet.

601   In Fig. 12(e), it is observed that the ejecting angle is increased from $\sim$ 15 degrees to $\sim$ 40

602   degrees as the ambient pressure decreases from 1 bar (1×10^5 Pa) to 10 mbar (1×10^3 Pa). This is

603   because the vapor jet expansion is subject to less confinement at lower pressure levels (Fig. 5(c)).

36

604   As a result, the vapor jet expands at a larger diverging angle and causes a larger ejecting angle for

605   the ejected particles. This trend also agrees with the findings in [12]. As the ambient pressure

606   increases from 1 bar (1×10^5 Pa) to 5 bar (5×10^5 Pa), the ejecting angle dramatically increases due

607   to the increasingly frequent occurrence of recoil-mode ejection. The recoil-mode ejection can

608   cause a large ejecting angle, even larger than 90 degrees, when the particle is ejected downwards

609   to the powder bed (e.g., Particle 7 in Fig. 9).

610

611   **4. Discussion on Powder Motion Mitigation**

612   The simulation results show that a high ambient pressure can significantly suppress the gas

613   flow (**Fig. 6**), and therefore, reduce the drag forces (**Fig. 12**(a)) and the occurrences of powder

614   entrainment and ejection (**Fig. 12**(b)). This suggests that applying of a high ambient pressure can

615   be an effective way to mitigate powder motion. The effects of hyper-atmospheric conditions (3 bar

616   and 5 bar) have been experimentally investigated in [14] with a moving laser. The authors found

617   that the number of entrained particles decreases with the ambient pressure, which agrees with the

618   current simulation results. However, the authors also found that the number of ejected particles

619   increases with the ambient pressure, which is different from the current simulation results for a

620   stationary laser. This discrepancy can be explained as follows. In a stationary-laser process under

621   high ambient pressure, the particles illuminated by the laser beam center are melted and merged

622   into the molten pool, and the particles outside the laser illumination will not have significant

623   motion because the gas flow is suppressed under high ambient pressure. Only the particles

624   illuminated by the rim of the laser can potentially be ejected by the recoil-mode ejection (**Fig. 10**).

625   As the number of particles in the rim of the laser is low for a stationary laser, few particle ejection

626   events are possible. And if those particles are successfully ejected, no more particles will be

627   entrained to the rim of the laser and then be ejected, so the powder ejection will not continue. The

628   situation is very different with a moving laser. As the laser moves along a given contour, it

629   constantly catches new particles in its moving rim. All the particles on the laser scanning contour

630   will be caught by the rim of the laser at certain moments and likely be ejected by the recoil-mode

631   ejection. Therefore, the high ambient pressure may not reduce the powder ejection in a moving-

632   laser case, and under the conditions in [14], the high ambient pressure even increases the powder

633   ejection. Moreover, the ejected particles under high ambient pressure are typically in a molten state

634   (**Fig. 12**(d)) and have a large divergence angle (**Fig. 12**(e)). They can stick with other particles to

635   form agglomerates, which can grow through a "snow-balling" mechanism [5], that the

636   agglomerates can be later ejected again and stick with more particles. This is confirmed in [14],

637   where the authors found more powder spatter with larger size and temperature under high ambient

638   pressure conditions.

639   Based on the above reasoning, we propose a new strategy that can potentially mitigate the

640   powder motion in a moving-laser process: applying a high ambient pressure along with a pulsed

641   laser beam. The pulsed laser beam moves in consecutive points and remains at each point for a

642   certain amount of time (exposure time) before moving to the next point. We expect two beneficial

643   effects from this strategy: (1) only the particles illuminated by the rim of the laser beam of each

644   pulse can be ejected by the recoil-mode ejection. Therefore, the number of potential ejected

645   particles is reduced compared to the continuous moving laser. (2) the point distance between two

646   consecutive points and the exposure time can be optimized to further reduce powder ejection. For

647   example, the point distance and exposure time can be adjusted so that the particles at the rim of

648   the previous pulse will fall in the center of the next pulse before they can be ejected.

649   It is noted that the use of pulsed laser beam in LPBF has been reported in the literature [36-

650   39], but the laser pulsating is used to control the molten pool stability, the cooling rate, and the

651   microstructure. To the best of our knowledge, the effects of pulsed laser on the powder motion

652   have not been investigated. It is also emphasized that a pulsed laser can only effectively mitigate

653   powder motion in a high ambient pressure. Under medium and low ambient pressure levels,

654   surrounding particles will continuously move toward the rim of the laser through the entrainment

655   mode and then be ejected through the elevation or expulsion modes. In the future, we will perform

656   X-ray imaging experiments and numerical simulations to examine the effectiveness of this

657   proposed strategy.

658

659   **5. Conclusion**

660   In this work, a 3D multiphysics model is developed that fully couples the molten pool

661   dynamics, gas flow, and powder motion in LPBF. The model capabilities highlight in resolving

662   the gas flow surrounding the powder particles, as well as quantifying the forces exerted on the

663   particle surfaces. In a "spot-welding" setup, simulations are carried out to investigate the effects

664   of the ambient pressure (in the range of 10 mbar – 5 bar) on the gas flow, powder-gas interaction,

665   and powder behavior. The temperature, flow velocity, and pressure field in the gas under different

666   ambient pressure levels are first quantified. Then, characteristic powder motions are examined and

667   explained by the powder-gas interaction mode(s). Finally, the powder behavior (e.g., velocity,

668   temperature, and ejecting angle) is statistically analyzed as a function of the ambient pressure. The

669   model predictions of powder motion agree well with the high-speed X-ray imaging experiments.

670   A consistent gas flow pattern is observed in simulations for all ambient pressure levels

671   investigated. The vapor jet initiates from the DZ and expands into the ambient, while the ambient

672   gas is entrained towards the LIZ. The vapor jet expansion is driven by a pressure decrease from

673   the DZ bottom towards the DZ opening. The entrainment flow is driven by a pressure decrease

674   from the ambient towards the LIZ. As the ambient pressure decreases from 5 bar to 10 mbar, the

675   major effects on the gas flow are summarized as follows:

676   • The characteristic velocity of vapor jet expansion increases from 200 m/s to 1500 m/s. The

677   characteristic velocity of the entrainment flow increases from 5 m/s to 50 m/s.

678   • The divergent angle of the vapor jet expansion significantly increases.

679   • The characteristic temperature of the vapor jet decreases from 3400 K to 2100 K.

680   • The Knudsen number of the gas flow increases from the range (0.004 – 0.004) to the range

681   (0.05 – 0.5). The gas flow enters the slip flow regime (Kn > 0.01) when the ambient

682   pressure is about 1 bar. It is expected that the continuum assumption of the gas flow fails

683   ($Kn \gtrsim 0.2$) when the ambient pressure is below 10 mbar.

684   The four powder-gas interaction modes previously identified in the 2D simulations (i.e., recoil,

685   entrainment, elevation, and expulsion modes) are confirmed in the current 3D simulations. The

686   motion of a specific powder particle can be attributed to that the particle being subject to a single

687   powder-gas interaction mode or a sequence of modes. More knowledge regarding the interaction

688   modes and the resultant powder motion have been revealed with the 3D simulation results.

689   Specifically, the recoil mode is found as another cause for the powder ejection besides the

690   expulsion mode. Such recoil-mode ejection is mostly distinguished at ambient pressure levels

691   above 1 bar. New sequences of powder-gas interaction modes are also found at ambient pressure

692   levels below 400 mbar. The expulsion-elevation mode sequence causes the powder particle to

693   elevate after being ejected from the LIZ. The expulsion-entrainment-expulsion mode sequence

694   causes the particle to have a meandering motion.

695   From a statistical analysis, the major effects of the ambient pressure on the powder-related

696   quantities are summarized as follows:

697   • The number of ejected particles monotonically increases as the ambient pressure is

698   decreased.

699   • The ejection drag force on the particle has a magnitude of $10^{-6} – 10^{-5}$ N. It is the maximum

700   when the ambient pressure is at a medium level (~ 1 bar). The entrainment drag force has

701   a magnitude of $10^{-7} – 10^{-6}$ N and also peaks at ~ 1 bar. The recoil force has a magnitude of

702   ~ 10^{-5} N and does not significantly change with the ambient pressure.

703   • The ejection velocity of the particle is about 2 – 4 m/s. The entrainment velocity is about

704   0.5 m/s. For both velocities, the maximum velocity is achieved at ~ 400 mbar.

705   • The temperature of the ejected particles monotonically increases from ~ 500 K to ~ 3500

706   K, as the ambient pressure is increased from 10 mbar to 5 bar.

707   The current 3D model provides quantitative information regarding the gas flow, powder-gas

708   interaction, and powder behavior. Based on the above information, we propose that implementing

709   a pulsed laser under a high ambient pressure can reduce the powder motion in LPBF.

710

711   **Appendix A: Tracking powder-related quantities for simulations and experiments**

712   For each powder particle in the simulation, the angular velocity, torque, velocity, forces (F_p

713   and F_v), and average temperature can be tracked with respect to time. The tracking of Particles 1

714   – 5 in Fig. 8 is given in Fig. A1, and the tracking of Particles 6 – 9 in Fig. 9 is given in Fig. A2, as

715   examples. F_p is the force (magnitude) integrated by the pressure distribution (including recoil

716   pressure if evaporation occurs) on the particle surface. F_v is the force (magnitude) integrated by

717   the viscous stress distribution on the particle surface. These integrations are performed numerically

718   using the "Lagrangian points" [26] on the particle surface. The average temperature of the particle

719   is calculated by averaging the temperature of the cells inside a particle from the CFD computation.

720   The particle tracking is terminated once the particle moves out of the calculation domain or merges
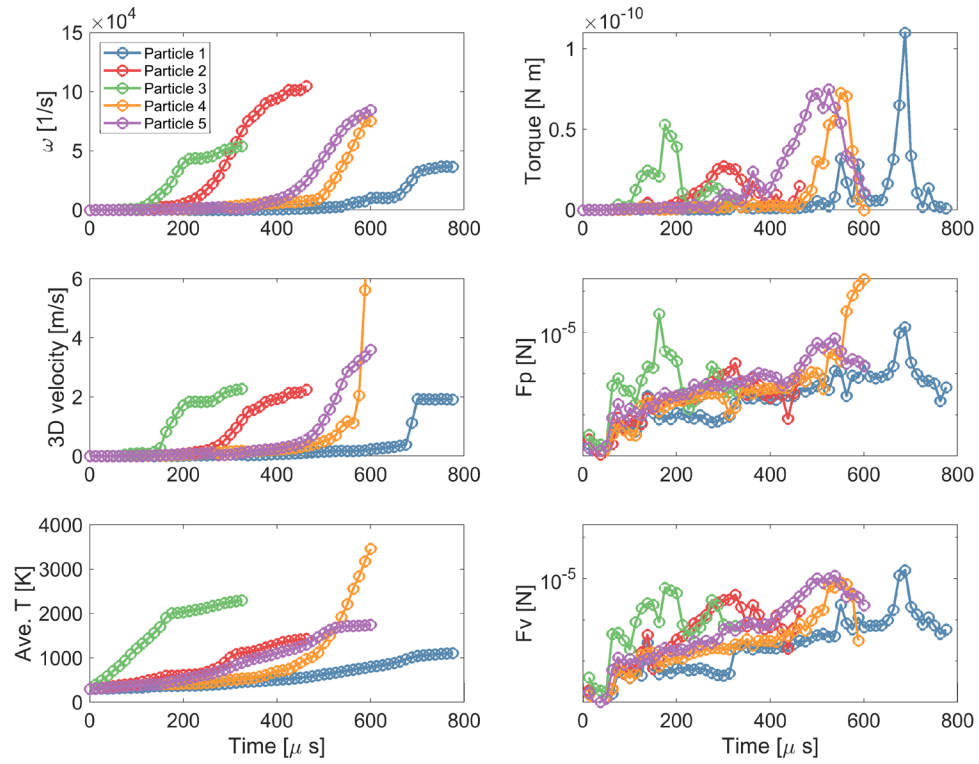
721   into the molten pool.

723   **Fig. A1. Tracking of the angular velocity, torque, velocity, forces, and average temperature**
724   **of Particles 1 – 5 (in Fig. 8) with respect to time.**
725
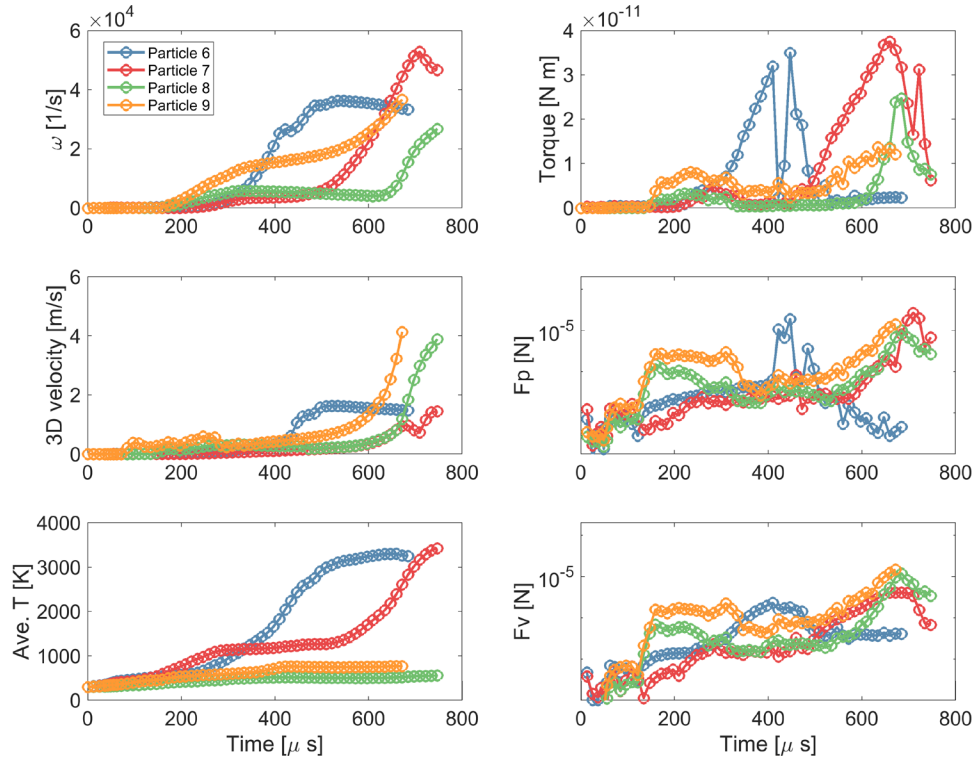
Fig. A2. Tracking of the angular velocity, torque, velocity, forces, and average temperature of Particles 6 – 9 in (Fig. 9) with respect to time.

The projected particle trajectories are manually extracted from the high-speed X-ray imaging, and the projected particle velocities can be calculated from the particle trajectories. Examples are shown in Fig. A3. The maximum projected velocities in a particle's lifespan are comparable to the velocity magnitude (0.5 – 3 m/s) shown in Fig. 12(c).
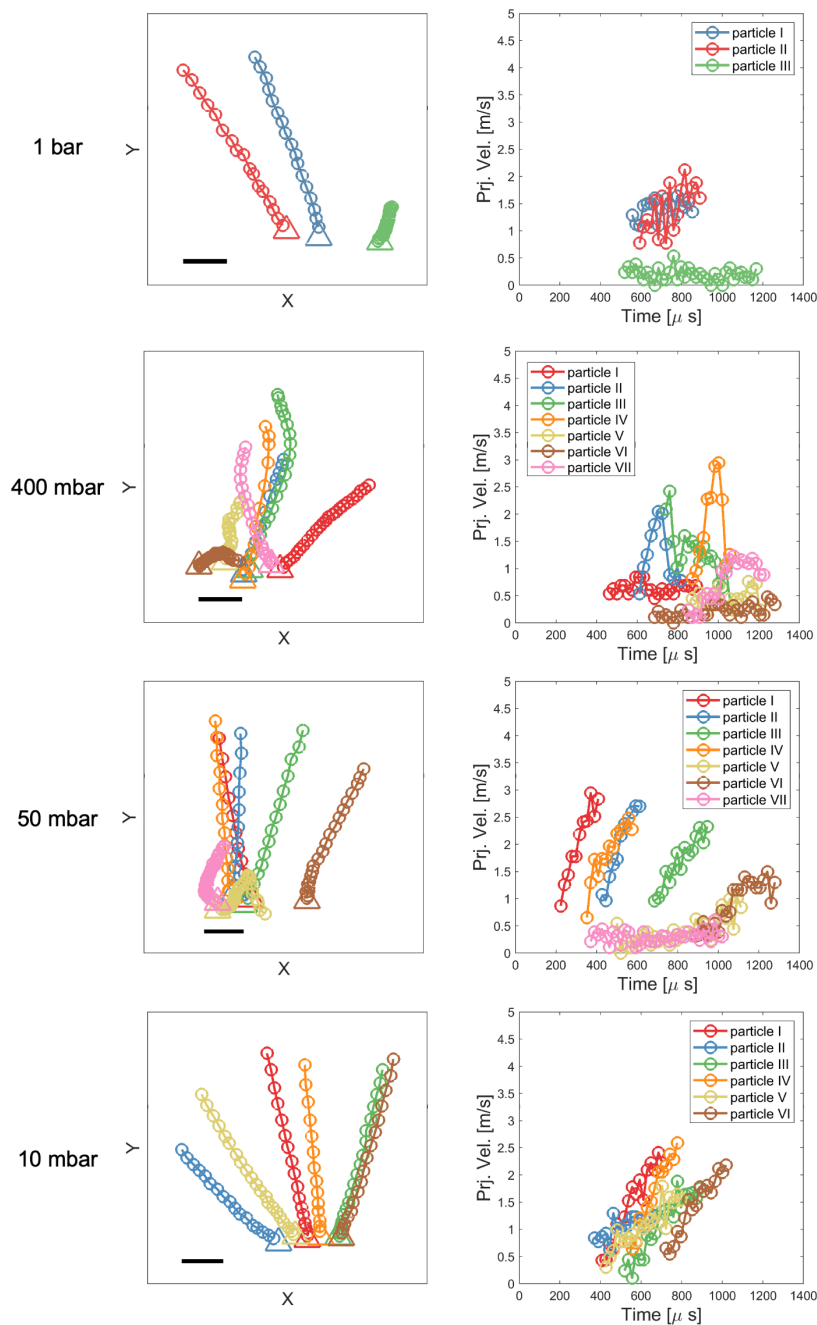
43

Fig. A3. Typical projected particle trajectories and velocities manually tracked from high-speed X-ray imaging results. All scale bars are 100 μm.

Appendix B: Details on statistical quantification of powder behavior

For each simulation, The "entrained particle" and the "ejected particle" are defined as follows. If a powder particle moves towards the LIZ from the X-Z projection view, e.g., Fig. 8(b) and Fig. 9(b), for a projected distance larger than 50 μm, it is defined as an entrained particle. If a particle moves away from the LIZ for a distance larger than 50 μm (not projected distance), it is defined as an ejected particle. It is noted a particle can be both an entrained particle and an ejected particle.

For each entrained particle, the projected (X-Z plane) drag force on the particle when it is entrained (i.e., moving towards the LIZ) is defined as the "entrainment drag." For each ejected particle, the drag force (not projected) on the particle when it is ejected (i.e., moving away from the LIZ) is defined as the "ejection drag." For both the entrained and ejected particle, the recoil force is defined as the force (not projected) exerted on the particle by the recoil pressure if there is any evaporation occurs on the particle surface. Based on these definitions, we can identify the maximum entrainment drag, ejection drag, and recoil force for each entrained/ejected particle during its lifespan. Finally, we average these maximum forces over all entrained/ejected particles in the simulations and plot the averaged value in Fig. 12(a). The range of these maximum forces is indicated by the error bars in Fig. 12(a). The occurrences of the entrained and ejected particles are normalized by the total amount of particles in the powder bed, as shown in Fig. 12(b).

In Fig. 12(c), the entrainment and ejection velocities are defined as follows. For each entrained particle, the projected (X-Z plane) velocity when the particle is entrained is defined as the "entrainment velocity." For each ejected particle, the velocity (not projected) when the particle is ejected is defined as the "ejection velocity." Based on these definitions, we can identify the maximum entrainment and ejection velocity for each entrained/ejected particle during its lifespan.

761   Finally, we average these maximum velocities over all entrained/ejected particles in the

762   simulations and plot the averaged values in Fig. 12(c).

763   For each ejected particle, we can identify the maximum particle (average) temperature when

764   it is ejected. We average the maximum particle temperature over all ejected particles and plot the

765   averaged values in Fig. 12(d). Also, for each ejected particle, the last simulated moment when the

766   particle is ejected is used to calculate the ejecting angle. The ejecting angle is calculated by

767    $\mathrm{acos}(v_y/v)$, where v is the particle velocity magnitude and v_y is the vertical component of

768   velocity. We average the ejecting angle over all the ejected particles and plot the averaged values

769   in Fig. 12(e).

770

References

[1]   S. Ly, A. M. Rubenchik, S. A. Khairallah, G. Guss, and M. J. Matthews, "Metal vapor micro-jet controls material redistribution in laser powder bed fusion additive manufacturing," *Scientific reports,* vol. 7, no. 1, p. 4085, 2017.

[2]   P. Bidare, I. Bitharas, R. Ward, M. Attallah, and A. Moore, "Fluid and particle dynamics in laser powder bed fusion," *Acta Materialia,* vol. 142, pp. 107-120, 2018.

[3]   C. Zhao *et al.*, "Real-time monitoring of laser powder bed fusion process using high-speed X-ray imaging and diffraction," *Scientific reports,* vol. 7, no. 1, p. 3602, 2017.

[4]   M. J. Matthews, G. Guss, S. A. Khairallah, A. M. Rubenchik, P. J. Depond, and W. E. King, "Denudation of metal powder layers in laser powder bed fusion processes," *Acta Materialia,* vol. 114, pp. 33-42, 2016.

[5]   Z. A. Young *et al.*, "Types of spatter and their features and formation mechanisms in laser powder bed fusion additive manufacturing process," *Additive Manufacturing,* vol. 36, p. 101438, 2020.

[6]   U. Ali *et al.*, "Identification and characterization of spatter particles and their effect on surface roughness, density and mechanical response of 17-4 PH stainless steel laser powder-bed fusion parts," *Materials Science and Engineering: A,* vol. 756, pp. 98-107, 2019.

[7]   S. A. Khairallah *et al.*, "Controlling interdependent meso-nanosecond dynamics and defect generation in metal 3D printing," *Science,* vol. 368, no. 6491, pp. 660-665, 2020.

[8]   M. Simonelli *et al.*, "A study on the laser spatter and the oxidation reactions during selective laser melting of 316L stainless steel, Al-Si10-Mg, and Ti-6Al-4V," *Metallurgical and Materials Transactions A,* vol. 46, no. 9, pp. 3842-3851, 2015.

[9]   A. T. Polonsky and T. M. Pollock, "Closing the science gap in 3D metal printing," *Science,* vol. 368, no. 6491, pp. 583-584, 2020.

[10]   D. Wang *et al.*, "Influence of spatter particles contamination on densification behavior and tensile properties of CoCrW manufactured by selective laser melting," *Optics & Laser Technology,* vol. 121, p. 105678, 2020.

[11]   L. E. Criales, Y. M. Arısoy, B. Lane, S. Moylan, A. Donmez, and T. Özel, "Laser powder bed fusion of nickel alloy 625: experimental investigations of effects of process parameters

on melt pool size and shape with spatter analysis," *International Journal of Machine Tools and Manufacture,* vol. 121, pp. 22-36, 2017.

[12] Q. Guo *et al.*, "Transient dynamics of powder spattering in laser powder bed fusion additive manufacturing process revealed by in-situ high-speed high-energy x-ray imaging," *Acta Materialia,* vol. 151, pp. 169-180, 2018.

[13] P. Bidare, I. Bitharas, R. M. Ward, M. M. Attallah, and A. J. Moore, "Laser powder bed fusion at sub-atmospheric pressures," *International Journal of Machine Tools and Manufacture,* vol. 130, pp. 65-72, 2018.

[14] P. Bidare, I. Bitharas, R. M. Ward, M. M. Attallah, and A. J. Moore, "Laser powder bed fusion in high-pressure atmospheres," *The International Journal of Advanced Manufacturing Technology,* vol. 99, no. 1-4, pp. 543-555, 2018.

[15] S. Traore *et al.*, "Influence of gas atmosphere (Ar or He) on the laser powder bed fusion of a Ni-based alloy," *Journal of Materials Processing Technology,* vol. 288, p. 116851, 2020.

[16] C. Pauzon, P. Forêt, E. Hryha, T. Arunprasad, and L. Nyborg, "Argon-helium mixtures as Laser-Powder Bed Fusion atmospheres: Towards increased build rate of Ti-6Al-4V," *Journal of Materials Processing Technology,* vol. 279, p. 116555, 2020.

[17] I. Bitharas, A. Burton, A. J. Ross, and A. J. Moore, "Visualisation and numerical analysis of laser powder bed fusion under cross-flow," *Additive Manufacturing,* p. 101690, 2020.

[18] L. Kaserer, S. Bergmueller, J. Braun, and G. Leichtfried, "Vacuum laser powder bed fusion—track consolidation, powder denudation, and future potential," *The International Journal of Advanced Manufacturing Technology,* vol. 110, no. 11, pp. 3339-3346, 2020.

[19] C. Tang, K. Q. Le, and C. H. Wong, "Physics of humping formation in laser powder bed fusion," *International Journal of Heat and Mass Transfer,* vol. 149, p. 119172, 2020.

[20] M. Bayat *et al.*, "Keyhole-induced porosities in Laser-based Powder Bed Fusion (L-PBF) of Ti6Al4V: High-fidelity modelling and experimental validation," *Additive Manufacturing,* vol. 30, p. 100835, 2019.

[21] S. A. Khairallah, A. T. Anderson, A. Rubenchik, and W. E. King, "Laser powder-bed fusion additive manufacturing: Physics of complex melt flow and formation mechanisms of pores, spatter, and denudation zones," *Acta Materialia,* vol. 108, pp. 36-45, 2016.

[22] W. Yan *et al.*, "Multi-physics modeling of single/multiple-track defect mechanisms in electron beam selective melting," *Acta Materialia,* vol. 134, pp. 324-333, 2017.

833 [23] A. Bauereiß, T. Scharowsky, and C. Körner, "Defect generation and propagation
834   mechanism during additive manufacturing by selective beam melting," *Journal of*
835   *Materials Processing Technology,* vol. 214, no. 11, pp. 2522-2528, 2014.

836 [24] Y. A. Mayi *et al.*, "Laser-induced plume investigated by finite element modelling and
837   scaling of particle entrainment in laser powder bed fusion," *Journal of Physics D: Applied*
838   *Physics,* vol. 53, no. 7, p. 075306, 2019.

839 [25] H. Chen and W. Yan, "Spattering and denudation in laser powder bed fusion process:
840   multiphase flow modelling," *Acta Materialia,* vol. 196, pp. 154-167, 2020.

841 [26] X. Li, C. Zhao, T. Sun, and W. Tan, "Revealing transient powder-gas interaction in laser
842   powder bed fusion process through multi-physics modeling and high-speed synchrotron x-
843   ray imaging," *Additive Manufacturing,* vol. 35, p. 101362, 2020.

844 [27] N. Kouraytem *et al.*, "Effect of Laser-Matter Interaction on Molten Pool Flow and Keyhole
845   Dynamics," *Physical Review Applied,* vol. 11, no. 6, p. 064054, 2019.

846 [28] W. Tan, N. S. Bailey, and Y. C. Shin, "Investigation of keyhole plume and molten pool
847   based on a three-dimensional dynamic model with sharp interface formulation," *Journal of*
848   *Physics D: Applied Physics,* vol. 46, no. 5, p. 055501, 2013.

849 [29] W. Tan and Y. C. Shin, "Analysis of multi-phase interaction and its effects on keyhole
850   dynamics with a multi-physics numerical model," *Journal of Physics D: Applied Physics,*
851   vol. 47, no. 34, p. 345501, 2014.

852 [30] R. L. Panton, *Incompressible flow*. John Wiley & Sons, 2013.

853 [31] G. A. Bird and J. M. Brady, *Molecular gas dynamics and the direct simulation of gas flows*.
854   Clarendon press Oxford, 1994.

855 [32] W. S. Jodrey and E. M. Tory, "Simulation of random packing of spheres," *Simulation,* vol.
856   32, no. 1, pp. 1-12, 1979.

857 [33] K. C. Mills, *Recommended values of thermophysical properties for selected commercial*
858   *alloys*. Woodhead Publishing, 2002.

859 [34] C. S. Kim, "Thermophysical properties of stainless steels," Argonne National Lab.,
860   Ill.(USA), 1975.

861 [35] P. Pichler, B. J. Simonds, J. W. Sowards, and G. Pottlacher, "Measurements of
862   thermophysical properties of solid and liquid NIST SRM 316L stainless steel," *Journal of*
863   *Materials Science,* vol. 55, no. 9, pp. 4081-4093, 2020.

864 [36] S. C. Chou, M. Trask, J. Danovitch, X. L. Wang, J. P. Choi, and M. Brochu, "Pulsed laser
865 powder bed fusion additive manufacturing of A356," *Materials Characterization,* vol. 143,
866 pp. 27-33, 2018.

867 [37] A. G. Demir, L. Mazzoleni, L. Caprio, M. Pacher, and B. Previtali, "Complementary use
868 of pulsed and continuous wave emission modes to stabilize melt pool geometry in laser
869 powder bed fusion," *Optics & Laser Technology,* vol. 113, pp. 15-26, 2019.

870 [38] K. Georgilas, R. H. U. Khan, and M. E. Kartal, "The influence of pulsed laser powder bed
871 fusion process parameters on Inconel 718 material properties," *Materials Science and*
872 *Engineering: A,* vol. 769, p. 138527, 2020.

873 [39] M. Zavala-Arredondo *et al.*, "Use of power factor and specific point energy as design
874 parameters in laser powder-bed-fusion (L-PBF) of AlSi10Mg alloy," *Materials & Design,*
875 vol. 182, p. 108018, 2019.
876